

Computational Science
Laboratory Report CSL-TR-25-3
May 2, 2025

Amit N Subrahmanya, Adrian Sandu

*“Feature preserving data assimilation via
feature alignment”*

Computational Science Laboratory
“Compute the Future!”

Department of Computer Science
Virginia Tech

Blacksburg, VA 24060

Phone: (540) 231-2193

Fax: (540) 231-6075

Email: amitns@vt.edu, sandu@vt.edu

Web: <https://cs1.cs.vt.edu>



Feature preserving data assimilation via feature alignment

Amit N. Subrahmanya^{a,*}, Adrian Sandu^a

^a*Computational Science Laboratory, Department of Computer Science, Virginia Tech, 620 Drillfield Dr., Blacksburg, 24061, Virginia, USA*

Abstract

Data assimilation combines information from physical observations and numerical simulation results to obtain better estimates of the state and parameters of a physical system. A wide class of physical systems of interest have solutions that exhibit the formation of structures, called features, which have to be accurately captured by the assimilation framework. For example, fluids can develop features such as shockwaves and contact discontinuities that need to be tracked and preserved during data assimilation. State-of-the-art data assimilation techniques are agnostic of such features. Current ensemble-based methods construct state estimates by taking linear combinations of multiple ensemble states; repeated averaging tends to smear the features over multiple assimilation cycles, leading to nonphysical state estimates. A novel feature-preserving data assimilation methodology that combines sequence alignment with the ensemble transform particle filter is proposed to overcome this limitation of existing assimilation algorithms. Specifically, optimal transport of particles is performed along feature-aligned characteristics. The strength of the proposed feature-preserving filtering approach is demonstrated on multiple test problems described by the compressible Euler equations.

Keywords: Bayesian Inference, Data Assimilation, Particle Filters, Compressible Flow Control, Shock Preservation

*Corresponding author

Email addresses: amitns@vt.edu (Amit N. Subrahmanya), asandu7@vt.edu (Adrian Sandu)

1. Introduction

Data assimilation combines information from noisy observations of physical phenomena and numerical simulations of the said phenomena to obtain improved estimates of the system state and parameters [1–4]. While data assimilation originated in the numerical weather prediction community, it has successfully been applied across various fields, including geosciences, environmental sciences [1], pandemic modelling [3], etc. Data assimilation is formulated in the Bayesian framework, where the prior probability given by the numerical simulation (and its associated uncertainty) is combined with the likelihood of the observation data conditioned by the system state [3]. The result is the posterior probability density that describes an observation-informed understanding of the physical phenomena (compared to the uninformed prior).

This work considers the discrete-time data assimilation problem for systems modeled by the compressible Euler equations [5]. These systems can exhibit abrupt transitions in flow properties such as density, pressure, and energy, in the form of shock waves, contact discontinuities, and other features. Here, the term *feature* refers to any coherent abrupt transition in the physical field that forms a characteristic structure or profile in the solution. We seek to construct data assimilation methodologies that are feature-aware, and provide physically faithful state estimates that preserve the features of the solution.

Modern ensemble-based data assimilation methods use a Monte-Carlo approach to represent uncertainties via samples (called ensemble members or particles), thus bypassing difficulties associated with the representation of probability densities in high-dimensional problems. The ensemble Kalman filter [6] (EnKF), and its numerous variants [1, 7–9], are expected to show optimal performance when the uncertainties are well approximated by a Gaussian density. However, in the presence of discontinuous features, the Gaussian approximation breaks down as the states on different sides of a discontinuity are uncorrelated.

For this reason, particle filters [10, 11], which make no specific assumption about the underlying distribution, offer a more promising approach for systems with features. The traditional particle filter represents the importance of each sample with an associated weight; when new observations become available, the weights are updated based on the likelihood of the data with respect to the particle state. The states are not modified during the assimilation phase, which preserves the solution features of each particle. Unfortunately, over multiple assimilation instances, weight degeneracy [11]—where few particles have large weights rendering all other particles meaningless—becomes a problem. One way to alleviate degeneracy is by employing a large number of particles, but this is infeasible when the states are high-dimensional. A second way is by creating multiple perturbed copies of the highest weighted particles and removing the lowest weighted particles. However, rigorously resampling particles with features is itself an open question.

An alternative approach to alleviate the weight degeneracy problem is to employ particle filters that also modify particle states, as follows. (i) Proposal density particle filters [11, 12] generate samples from distributions that are similar in some regard to the posterior, thereby reducing weight degeneracy. However, resampling for states while preserving features can be an arduous task. (ii) Particle flow filters [13–15] move particles in state space toward the posterior under the flow of a stochastic differential equation. Particle flow filters can be modified to handle equality constraints [16], but it is difficult to represent discontinuous features as an enforceable constraint. (iii) The ensemble transform particle filter (ETPF) [2, 17] solves a linear program minimizing the discrete Wasserstein-1 distance to transport unequally weighted analysis particles to equally weighted particles. Standard ETPF does not preserve features, as posterior particles are linear combinations of prior particles that average out solution structures. In this work, we propose a modified ETPF that preserves features.

Previous work on feature-preserving data assimilation. Scant literature exists on preserving discontinuous features for the state estimation problem. One of

the earliest works we found on resolving sharp features in data assimilation was by Freitag et. al. [18]. The authors modify the traditional 4DVar cost function with L_1 norm and mixed $L_1 - L_2$ norm penalty terms to account for features in the linear advection equation. Next, Srivastava et. al. [19] formulate a feature-informed data assimilation framework where features are extracted using a level-set approach to modify the parameters (but not the states) of the numerical model. Li. et. al. [20] modify the prior covariance (essentially, a different type of localization) in the ensemble Kalman filter to obtain a feature-consistent ensemble mean for the 1D shallow water equations while observing every other state. Houba et. al. [21] study multiple filters such as the extended Kalman filter (EKF), EnKF, and the sequential importance resampling particle filter for feature-preserving data assimilation. They demonstrate the difficulty of this problem where features smooth out for the EKF and EnKF. In specific circumstances, EnKF results in non-physical (i.e. negative) pressure, which causes the numerical model to fail to evolve the states further in time. The particle filter shows promising performance, at the cost of resampling at the state of the initial condition and propagating the states to the assimilation time all over again to preserve features. Hansen et. al. [22] demonstrate the normal-score EnKF for feature preservation in a shock tube, which demonstrates better feature preservation than the EnKF. Edoh et. al. [23] make a positivity-preserving modification to the EnKF and apply it to compressible flows. The positivity-preserving transformation prevents EnKF from inferring non-physical pressures. The features are successfully captured, with some minimal smoothing. West et. al. [24] treat shock preservation as a variational parameter estimation problem, where the inferred parameters control the density and pressure on either side of the diaphragm in Sod’s shock tube setting at the initial time. This is computationally expensive as it requires expensive adjoint computations. More research is warranted to construct cost-efficient feature-preserving filters.

Contributions of this work. This work extends the ensemble transform particle filter (ETPF) to preserve solution features during assimilation. The new filtering

approach, named the “feature-preserving ETPF”, uses the following techniques: (i) **Feature extraction** where features (and their locations) are extracted from each of the particles using state information; (ii) **Aligned addition** where an aligned convex combination of two particles is realized by interpolation along feature-aligned characteristics, with the alignment realized via the dynamic time warping [25] method; (iii) **Feature-preserving ETPF** reformulates the ensemble transform of the ETPF method as a sequence of pairwise aligned additions, such that the resulting analyses respect the physical features of the solution. Feature extraction and alignment have been employed in data assimilation in other contexts such as hurricane or vortex location prediction [26–33]. While the methodology for the feature-aligned optimal transport was independently developed here, we learned that Operti [34] had previously used a combination of DTW and interpolation to predict the lithology of stratified rocks. We demonstrate the success of this approach on four different test problems in one and two dimensions.

Paper organization. The remainder of the paper is organized as follows. Section 2 reviews the compressible Euler equations (section 2.1), the data assimilation problem (section 2.2), the ensemble transform particle filter (section 2.3) and the dynamic time warping method (section 2.5). Section 3 describes feature extraction (section 3.1), feature-aligned addition (section 3.2) and the aligned ensemble transform particle filter (section 3.3). Section 4 illustrates the strength of the proposed algorithm on multiple experiments where features are successfully preserved. Finally, Section 5 presents the conclusions of the current work and our vision for future research.

2. Background

2.1. Compressible Euler equations

The prototypical example for systems that develop solutions with features is the compressible Euler system for an ideal polytropic gas [5], described by the

following set of partial differential equations:

$$\begin{aligned}\frac{\partial \rho}{\partial t} + \nabla \cdot (\rho \mathbf{u}) &= 0, \\ \frac{\partial \mathbf{u}}{\partial t} + \nabla \cdot (\rho \mathbf{u} \otimes \mathbf{u}) + \nabla p &= 0, \\ \frac{\partial E}{\partial t} + \nabla \cdot (\mathbf{u}(E + p)) &= 0.\end{aligned}\tag{1}$$

Here, ρ represents the density of the gas, \mathbf{u} represents the velocity vector in each spatial dimension, E represents the energy density, and p represents the pressure. When the system in eq. (1) is in thermodynamic equilibrium, the pressure p is given by the equation of state:

$$\frac{p}{\gamma - 1} = E - \frac{1}{2} |\mathbf{u}|^2,\tag{2}$$

where γ is the adiabatic constant of the gas. An additional quantity of interest is the entropy of the system given by:

$$s = \log \left(\frac{p}{\rho^\gamma} \right).\tag{3}$$

For the remainder of the manuscript, the symbols $\rho, \mathbf{u}, E, p, s$ also refer to the respective physical variables after spatial discretization of eq. (1). This work deals with one-dimensional (in x) and two-dimensional (in x and y) discretizations of the Euler equations. In the next subsection, we introduce the data assimilation problem.

2.2. The data assimilation problem

In this work, the data assimilation problem aims to accurately track a partially observable gas dynamical physical system over time while preserving solution features. Formally, the latent true state for the gas dynamical physical system at discrete points in time t_k is represented by $\mathbf{x}_k^{\text{true}}$ where k indexes the time. For example, $\mathbf{x}_k^{\text{true}}$ could describe the infinite-dimensional physical fields of density, velocity, pressure, and energy density inside a shock tube. The

finite-dimensional observation (\mathbf{y}_k) of the latent state at discrete points in time t_k is obtained as:

$$\mathbf{y}_k = \tilde{\mathcal{H}}_k(\mathbf{x}_k^{\text{true}}) + \boldsymbol{\epsilon}_k, \quad \tilde{\mathcal{H}}_k : \mathbb{R}^\infty \rightarrow \mathbb{R}^{n_o}, \quad \boldsymbol{\epsilon}_k \sim \mathcal{P}_k^o \in \mathbb{R}^{n_o}, \quad (4)$$

where $\tilde{\mathcal{H}}_k$ is the physical observation operator, $\boldsymbol{\epsilon}_k$ is the additive observation error, and \mathcal{P}_k^o is the observation error density. The observations are assumed to be noisy due to inherent errors in measuring instruments. For example, pressure sensors could be placed inside a shock tube to acquire pressure data.

Data assimilation seeks to estimate the discretized finite-dimensional state $\mathbf{x}_k = [\rho_k, \mathbf{u}_k, E_k] \in \mathbb{R}^{n_s}$ from a computational model to approximate the latent true state $\mathbf{x}_k^{\text{true}}$. For example, the model could be a computational fluid dynamics solver simulating a shock tube. The state \mathbf{x}_{k-1} is evolved to \mathbf{x}_k through a deterministic computational model \mathcal{M}_k as follows:

$$\mathbf{x}_k = \mathcal{M}_k(\mathbf{x}_{k-1}), \quad \mathcal{M}_k : \mathbb{R}^{n_s} \rightarrow \mathbb{R}^{n_s}. \quad (5)$$

\mathbf{x}_k is modeled as a random variable with probability density $\mathcal{P}_k(\mathbf{x})$ due to uncertainty in both (i) the initial estimate for $\mathbf{x}_0^{\text{true}}$; and (ii) the model dynamics \mathcal{M} , which weakly approximates the dynamics of the physical system. The specific implementation details of the model operator \mathcal{M} , concerning the discretization of the system in eqs. (1) and (2) are discussed in Section 4.

While direct comparison of \mathbf{x}_k with $\mathbf{x}_k^{\text{true}}$ is impossible, comparison between the physical observation \mathbf{y}_k and the numerical observation $\mathbf{z}_k \in \mathbb{R}^{n_o}$ is possible. \mathbf{z}_k is obtained from the numerical observation operator \mathcal{H}_k as

$$\mathbf{z}_k = \mathcal{H}_k(\mathbf{x}_k), \quad \mathcal{H}_k : \mathbb{R}^{n_s} \rightarrow \mathbb{R}^{n_o}. \quad (6)$$

For example, if the physical observation \mathbf{y}_k (from eq. (4)) gathers pressure data from a set of locations within a shock tube, then the numerical observation \mathbf{z}_k (from eq. (6)) calculates the pressure at the same set of locations from \mathbf{x}_k (which is the numerically computed pressure field of shock tube simulation). In

realistic scenarios, physical measurements are expensive and difficult to obtain, resulting in extremely low-dimensional observations compared to the size of model discretization, i.e., $n_o \ll n_s$.

Filtering data assimilation entails the application of the following sequence of two steps at every time instance:

- (i) forecasting, which runs the model starting from the previous analysis $\mathbf{x}_k^f = \mathcal{M}_k(\mathbf{x}_{k-1}^a)$, to obtain a model prediction \mathbf{x}_k^f with the corresponding probability density $\mathcal{P}_k^f(\mathbf{x})$; and
- (ii) analysis, which computes the current analysis state \mathbf{x}_k^a and its probability density $\mathcal{P}_k^a(\mathbf{x})$ by correcting the model prediction with the new observation information.

The analysis (or posterior) density is modeled according to Bayes' rule as

$$\mathcal{P}_k^a(\mathbf{x}) \propto \mathcal{P}_k^o(\mathbf{y}|\mathbf{x}) \mathcal{P}_k^f(\mathbf{x}), \quad (7)$$

with the observational likelihood $\mathcal{P}_k^o(\mathbf{y}|\mathbf{x})$ and forecast (or prior) density $\mathcal{P}_k^f(\mathbf{x})$. The probability densities are approximated in a Monte-Carlo fashion by n_e samples, called particles:

$$\mathbf{X}_k = \begin{bmatrix} \mathbf{x}_k^{[1]} & \mathbf{x}_k^{[2]} & \dots & \mathbf{x}_k^{[n_e]} \end{bmatrix} \in \mathbb{R}^{n_s \times n_e}, \quad (8)$$

where each particle is a realization of the model state random variable $\mathbf{x}_k \in \mathbb{R}^{n_s}$. Note that, with a slight abuse of notation, \mathbf{x} denotes both the random variable and its realization. The set of particles is paired with a weight vector representing the relative importance of each particle. Formally, the weights are given by

$$\mathbf{w}_k = \begin{bmatrix} w_k^{[1]} & w_k^{[2]} & \dots & w_k^{[n_e]} \end{bmatrix} \in \mathbb{R}^{n_e}, \quad (9)$$

with the additional property that $\sum_{e=1}^{n_e} w_k^{[e]} = 1$. The particles and weights

define the empirical probability density:

$$\mathcal{P}_k(\mathbf{x}) = \sum_{e=1}^{n_e} w_k^{[e]} \delta(\mathbf{x} - \mathbf{x}_k^{[e]}), \text{ where } \delta(\mathbf{x}) = \begin{cases} \infty & \text{if } \mathbf{x} = \mathbf{0}, \\ 0 & \text{otherwise,} \end{cases} \quad (10)$$

In the prototypical particle filter—the bootstrap particle filter [11]—the particle states evolve in the forecast step, but the weights remain constant:

$$\begin{aligned} \mathcal{P}_{k-1}^a(\mathbf{x}) &= \sum_{e=1}^{n_e} w_{k-1}^{a[e]} \delta(\mathbf{x} - \mathbf{x}_{k-1}^{a[e]}) \\ \xrightarrow{\mathbf{x}_k^{f[e]} = \mathcal{M}_k(\mathbf{x}_{k-1}^{a[e]})} \mathcal{P}_k^f(\mathbf{x}) &= \sum_{e=1}^{n_e} w_{k-1}^{a[e]} \delta(\mathbf{x} - \mathbf{x}_k^{f[e]}) \equiv \sum_{e=1}^{n_e} w_k^{f[e]} \delta(\mathbf{x} - \mathbf{x}_k^{f[e]}). \end{aligned} \quad (11)$$

Similarly, during the analysis step, the particle states remain unchanged, while the weights are modified. Given a prior density (11) described by forecast weights $w_k^{f[e]}$ and particles $\mathbf{x}_k^{f[e]}$, the bootstrap particle filter analysis is computed by Bayes' rule (eq. (7)) as

$$\begin{aligned} \mathcal{P}_k^a(\mathbf{x}) &= \frac{1}{C} \mathcal{P}_k^o(\mathbf{y}_k | \mathbf{x}) \sum_{e=1}^{n_e} \mathbf{w}_k^{f[e]} \delta(\mathbf{x} - \mathbf{x}_k^{f[e]}) \\ &= \sum_{e=1}^{n_e} \frac{\mathcal{P}_k^o(\mathbf{y}_k | \mathbf{x}_k^{f[e]}) \mathbf{w}_k^{f[e]}}{C} \delta(\mathbf{x} - \mathbf{x}_k^{f[e]}) \\ &\equiv \sum_{e=1}^{n_e} w_k^{a[e]} \delta(\mathbf{x} - \mathbf{x}_k^{f[e]}), \text{ with} \\ C &= \sum_{e=1}^{n_e} \mathcal{P}_k^o(\mathbf{y}_k | \mathbf{x}_k^{f[e]}) \mathbf{w}_k^{f[e]}. \end{aligned} \quad (12)$$

As is typical in data assimilation [3], the likelihood is calculated as $\mathcal{P}_k^o(\mathbf{y}_k | \mathbf{x}_k^{f[e]}) = \mathcal{P}_k^o(\mathbf{y}_k - \mathbf{z}_k^{f[e]})$. Here, the analysis particles are the same, i.e. $\mathbf{X}_k^a = \mathbf{X}_k^f$, but the analysis weights \mathbf{w}_k^a are modified. As the model in eq. (5) is deterministic, the weights do not change when the next forecast is made, i.e. $\mathbf{w}_{k+1}^f = \mathbf{w}_k^a$.

Performing this weight update over multiple assimilation cycles leads to weight degeneracy [11], where one or very few particles have dominant weights

and the other particles have negligible weights. This is not ideal for two reasons: (i) the particles with negligible weights result in wasted model computations, and (ii) the dominant (large weight) particles could stop being representative of the truth over time, simply because the state is never updated. To guard against weight degeneracy, one needs to either have an enormous number of particles or perform particle resampling such that the analysis particles all have equal weight. Traditional stochastic resampling is an expensive task for high-dimensional problems (large n_s), and feature preservation renders this task even more challenging. Alternatively, one can allow particle states to change during analysis, creating a different ensemble of particles with a more even distribution of weights; this process is interpreted as a deterministic resampling procedure. The ensemble transform particle filter [17], which uses such a deterministic resampling procedure, is discussed in the next section.

2.3. Ensemble transform particle filter

Based on transportation theory, the ETPF [17] formulates the deterministic resampling procedure as a discrete Kantorovich transportation problem [35]. Specifically, the ETPF (described in Algorithm 1) seeks to optimally transport the unequally weighted analysis ensemble to an equally weighted analysis ensemble. Because equally weighted analysis particles from time t_{k-1} are evolved to t_k , the forecast weights are all equal, i.e., $w_k^{\text{f}[e]} = \frac{1}{n_e}$ for all $e = \{1, \dots, n_e\}$, giving

$$w_k^{\text{a}[e]} = \frac{\mathcal{P}_k^{\text{o}}(\mathbf{y}_k - \mathbf{z}_k^{\text{f}[e]})}{\sum_{\varepsilon=1}^{n_e} \mathcal{P}_k^{\text{o}}(\mathbf{y}_k - \mathbf{z}_k^{\text{f}[\varepsilon]})}. \quad (13)$$

Any metric is a potential choice for \mathfrak{d} in Step 2 of Algorithm 1; in this work, it is the traditional L_2 norm: $\mathfrak{d}(\mathbf{x}_k^{\text{f}[i]}, \mathbf{x}_k^{\text{f}[j]}) = \|\mathbf{x}_k^{\text{f}[i]} - \mathbf{x}_k^{\text{f}[j]}\|_2$. In Step 4 Algorithm 1 returns equally weighted analysis particles $\mathbf{X}_k^{\text{a}} = \mathbf{X}_k^{\text{f}} \mathbf{T}^*$, whose states are convex combinations of the unequally weighted forecast particle states:

$$\mathbf{x}_k^{\text{a}[e]} = \sum_{j=1}^{n_e} \mathbf{T}_{j,e}^* \mathbf{x}_k^{\text{f}[j]}, \quad \mathbf{T}_{j,e}^* \geq 0, \quad \sum_{j=1}^{n_e} \mathbf{T}_{j,e}^* = 1, \quad e = 1, \dots, n_e. \quad (14)$$

For an in-depth discussion of ETPF, we refer the reader to the original work by Reich [17].

Algorithm 1 Ensemble transform particle filter at time t_k .

Require: Forecast ensemble $\mathbf{X}_k^f = \begin{bmatrix} \mathbf{x}_k^{f[1]} & \dots & \mathbf{x}_k^{f[n_e]} \end{bmatrix}$, observation \mathbf{y}_k .

- 1: Calculate analysis weights using eq. (13).
- 2: Calculate the distance matrix $\mathbf{D} \in \mathbb{R}^{n_e \times n_e}$ with the distance function \mathfrak{d} such that each element of \mathbf{D} is $\mathbf{D}_{i,j} = \mathfrak{d}(\mathbf{x}_k^{f[i]}, \mathbf{x}_k^{f[j]})$.
- 3: Solve the linear programming problem for the transform matrix \mathbf{T}^* :

$$\begin{aligned} \mathbf{T}^* = \arg \min_{\mathbf{T} \in \mathbb{R}^{n_e \times n_e}} \sum_{i,j=1}^{n_e} \mathbf{T}_{i,j} \mathbf{D}_{i,j} \\ \text{subject to } \mathbf{T}_{i,j} \geq 0, \quad \sum_i \mathbf{T}_{i,j} = \mathbf{1}_{n_e}^\top, \quad \sum_j \mathbf{T}_{i,j} = n_e \mathbf{w}^a. \end{aligned} \quad (15)$$

- 4: **return** $\mathbf{X}_k^a = \mathbf{X}_k^f \mathbf{T}^*$.
-

2.4. ETPF is challenged by systems with features

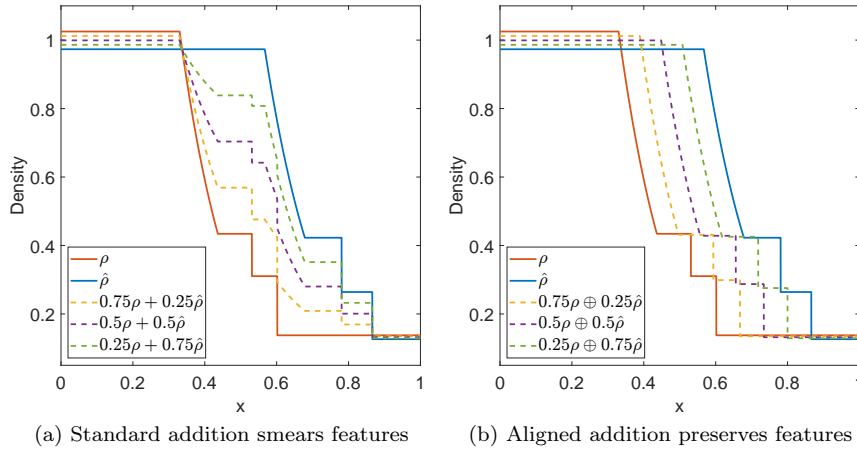


Figure 1: Convex combination of two different density profiles represented by the solid lines. Three different convex combinations are shown in the dashed lines. Aligned convex combination, depicted by \oplus for simplicity, is demystified in the following Section 3.2.

We now illustrate how the direct application of ETPF destroys features due to taking convex combinations of forecast particles (14). Consider two

particles with states \mathbf{x} and $\bar{\mathbf{x}}$ drawn from modified initial conditions on the Sod’s shock tube [36]; also see section 4.1, such that each particle state is a flow with features (at different locations. A convex combination of particles with a mixing coefficient α reads:

$$\bar{\mathbf{x}} = \alpha \mathbf{x} + (1 - \alpha) \hat{\mathbf{x}} \quad \text{where } 0 \leq \alpha \leq 1. \quad (16)$$

Each particle exhibits a rarefaction wave, a contact discontinuity, and a shock wave similar to the standard Sod’s shock tube test case. Figure 1 shows the density components (ρ and $\hat{\rho}$) of the two particles \mathbf{x} and $\hat{\mathbf{x}}$, and the density components $\bar{\rho}$ of $\bar{\mathbf{x}}$ (16) for three different mixing coefficients $\alpha = 0.75, 0.5, 0.25$ respectively. As seen in Figure 1a, the regular convex combination of the profiles using vector addition (16) results in the undesirable smearing of solution features.

The smearing can be avoided by adding along the feature-aligned characteristic of the two particles. The density component $\bar{\rho}$ of $\bar{\mathbf{x}}$ is obtained using the aligned convex combination of particle states as depicted in Figure 1b; the resulting $\bar{\mathbf{x}}$ shows feature preservation. In summary, aligned convex combinations result in particles with distinct features.

The aligned convex combination procedure and its application to the ETPF is discussed in Section 3. The aligned convex combination performs feature alignment using the dynamic time warping method [25, 37], which is briefly described next in Section 2.5.

2.5. Dynamic time warping

DTW has a long history of use in time series analysis [38], speech analysis [25, 39] to measure aligned similarity between univariate time series [40]. The authors view dynamic time warping as a framework to align generic sequences and, in the following discussion, treat it as such.

Following Tavenard [37], consider two univariate sequences

$$\zeta = [\zeta_1 \ \zeta_2 \ \dots \ \zeta_n] \in \mathbb{R}^n \quad \text{and} \quad \hat{\zeta} = [\hat{\zeta}_1 \ \hat{\zeta}_2 \ \dots \ \hat{\zeta}_m] \in \mathbb{R}^m$$

with $m, n \in \mathbb{N}$. An alignment seeks to optimally match elements from ζ and $\hat{\zeta}$ based on a design criterion while following certain mapping rules.

Specifically, an alignment is defined by a set of index pairs called an alignment path:

$$\pi = \{(i_1, \hat{i}_1), (i_2, \hat{i}_2), \dots, (i_\ell, \hat{i}_\ell)\} \subset \{\mathbb{N}_{\leq n} \times \mathbb{N}_{\leq m}\} \quad (17)$$

(here the alignment path has length ℓ). An index pair $\pi_v = (i_v, \hat{i}_v) \in \pi$ indicates that the i_v -th element of ζ is matched with the \hat{i}_v -th element of $\hat{\zeta}$ in the alignment π . The mapping rules for constructing the alignment path (17) are:

1. $\pi_1 = (i_1, \hat{i}_1) = (1, 1)$ indicating a match of the first elements;
2. $\pi_\ell = (i_\ell, \hat{i}_\ell) = (n, m)$ indicating a match of the last elements; and
3. For all $\pi_v = (i_v, \hat{i}_v)$ with $v \in \{2, \dots, \ell\}$ it holds that $i_{v-1} \leq i_v \leq i_{v-1} + 1$ and $\hat{i}_{v-1} \leq \hat{i}_v \leq \hat{i}_{v-1} + 1$. This indicates that the alignment indices form monotonically non-decreasing sequences, while also ensuring that every element from one sequence has at least one match in the other sequence. However, multiple consecutive elements in one sequence can have the same match in the other sequence.

The length of the alignment path (17) varies between $\max(m, n) \leq \ell \leq m+n-1$. The cardinality for the set of all alignment paths for ζ and $\hat{\zeta}$ that follow the mapping rules is given by the Delannoy number [37, 41]:

$$\sum_{v=0}^{\min(m,n)} \binom{m}{v} \binom{n}{v} 2^v. \quad (18)$$

For a given alignment path π (17) of length ℓ , the aligned q -norm distance

between the ζ and $\hat{\zeta}$ is defined as:

$$d(\pi, \zeta, \hat{\zeta}) = \left(\sum_{v=1}^{\ell} \left\| \zeta_{i_v} - \hat{\zeta}_{\hat{i}_v} \right\|^q \right)^{\frac{1}{q}}, \quad (19)$$

where $\| \cdot \|$ is a metric of the difference between individual elements of the two sequences (e.g., $|\cdot|$ if elements are scalars). DTW seeks to find the optimal alignment that minimizes the above distance (19) among all possible alignments of the sequences ζ and $\hat{\zeta}$, i.e.,

$$\pi^* = \arg \min_{\pi} d(\pi, \zeta, \hat{\zeta}). \quad (20)$$

This optimal distance $d(\pi^*, \zeta, \hat{\zeta})$ is the dynamic time warping distance. The optimal path length ℓ^* is a free variable determined during the optimization.

Remark 1. *Note that “aligned q -norm distance” eq. (19) does not obey the triangle inequality, and therefore is not a mathematically valid distance metric [37].*

While eq. (20) is a minimization over a finite set of solutions, it cannot be directly solved via enumeration due to the prohibitive resulting cost. An exact solution is obtained via dynamic programming [37] using the algorithm of Sakoe-Chiba [25]. While we consider the global alignment, one could also localize alignments if necessary by using the Sakoe-Chiba band [25] or the Itakura parallelogram [42]. Keogh et. al. [43] propose the derivative dynamic time warping (DDTW) method where discrete derivatives (finite difference) of the sequences are aligned, resulting in fewer many-to-one alignment mappings. It is possible to fix the length of the alignment path length ℓ^* (see [44]). For the implementation details, we refer the reader to the work by Sakoe and Chiba [25]; and Zhang et al. [44].

2.5.1. Multivariate DTW

While there are multiple extensions to DTW in the context of multivariate sequences [45–47], we focus on the dynamic image warping technique from

Hale [46] for this work. Specifically, given two matrices (seen as sequences in each dimension) to be aligned, Hale [46] formulates the two-dimensional DTW as sequence alignment in columns, followed by a sequence alignment in the rows. For this, consider two multivariate sequences of the same dimensions $\zeta \in \mathbb{R}^{n_{\text{row}} \times n_{\text{col}}}$, and $\hat{\zeta} \in \mathbb{R}^{n_{\text{row}} \times n_{\text{col}}}$ with $n_{\text{row}}, n_{\text{col}} \in \mathbb{N}$. Formally, the matrix ζ is viewed as a vector of columns and rows (in `MATLAB` notation) as

$$\zeta = \begin{bmatrix} \zeta_{:,1} & \zeta_{:,2} & \dots & \zeta_{:,n_{\text{col}}} \end{bmatrix} = \begin{bmatrix} \zeta_{1,:} \\ \zeta_{2,:} \\ \dots \\ \zeta_{n_{\text{row}},:} \end{bmatrix} \in \mathbb{R}^{n_{\text{row}} \times n_{\text{col}}}, \quad (21)$$

and $\hat{\zeta}$ is treated similarly. First, the columns are aligned, where the distance function from eq. (19) becomes

$$d(\pi_{\text{col}}, \zeta, \hat{\zeta}) = \left(\sum_{v=1}^{\ell_{\text{col}}} \left\| \zeta_{:,j_v} - \hat{\zeta}_{:,j_v^*} \right\|_2^q \right)^{\frac{1}{q}}. \quad (22)$$

Solving the DTW optimization (eq. (20)) with the distance function from eq. (22) produces the optimal column alignment path $\pi_{\text{col}}^* = \{(j_v^*, j_v)\}_{v=1}^{\ell_{\text{col}}}$ of cardinality ℓ_{col} . Next, eq. (20) is applied rowwise with the row-aligned distance function:

$$d(\pi_{\text{row}}, \zeta, \hat{\zeta}) = \left(\sum_{\iota=1}^{\ell_{\text{row}}} \left\| \zeta_{\iota,:} - \hat{\zeta}_{\iota,:} \right\|_2^q \right)^{\frac{1}{q}}. \quad (23)$$

to produce row alignment indices $\{(i_\iota^*, i_\iota)\}_{\iota=1}^{\ell_{\text{row}}}$ of cardinality ℓ_{row} . The complete optimal alignment path in 2D combines π_{col}^* and π_{row}^* as

$$\pi^* = \left\{ \left((i_\iota^*, j_v^*), (i_\iota, j_v) \right) \right\}_{\iota=1, v=1}^{\ell_{\text{row}}, \ell_{\text{col}}}, \quad (24)$$

indicating that the element $\zeta_{i_\iota^*, j_v^*}$ is mapped to $\hat{\zeta}_{i_\iota, j_v}$. In this work, the 2-norm is used for calculating distances, i.e., $q = 2$.

Remark 2. *It is possible to frame the two-dimensional cost function as*

$$d(\pi, \zeta, \hat{\zeta}) = \left(\sum_{\ell=1}^{\ell_{\text{row}}} \sum_{v=1}^{\ell_{\text{col}}} \left\| \zeta_{i_\ell, j_v} - \hat{\zeta}_{\hat{i}_\ell, \hat{j}_v} \right\|_2^q \right)^{\frac{1}{q}}, \quad (25)$$

with the added flexibility of differently sized matrices $\zeta \in \mathbb{R}^{n_{\text{row}} \times n_{\text{col}}}$, and $\hat{\zeta} \in \mathbb{R}^{m_{\text{row}} \times m_{\text{col}}}$ with $n_{\text{row}}, n_{\text{col}}, m_{\text{row}}, m_{\text{col}} \in \mathbb{N}$. This approach (explored in [45]) is not explored in this work due to the difficulty of the optimization problem.

3. Aligned Filtering Methodology

In this section, we discuss the aligned ensemble transform particle filter, which consists of: (i) extracting features from particle states; (ii) defining aligned convex combinations of particles; and (iii) deriving the feature-preserving ETPF, which modifies the ensemble transformation to account for feature alignments.

Without loss of generality, it is assumed that all particles are discretized on the same non-staggered, uniform, Cartesian grid. If particles violate the previous assumption, they can be interpolated onto a common, non-staggered, uniform, Cartesian grid, with appropriate treatment of boundary conditions, processed as described in this section, and interpolated back onto their original grids.

3.1. Feature Extraction

The goal is to identify and extract features from a particle discrete state $\mathbf{x} \in \mathbb{R}^{n_s}$. In the context of compressible Euler equations (Section 2.1), the state \mathbf{x} consists of the variables $[\rho, \mathbf{u}, E]$ discretized in one spatial dimension over the same uniform spatial grid. Features like shock waves and contact discontinuities can be detected by analyzing the density derivative. This is closely related to Schlieren photography [48], which identifies features by analyzing the refraction patterns of light rays moving through a compressible gas dynamical system, since the local refractive index of the gas changes with the local density. This is also related to edge detection methods from image processing [49]. The vector

notation ζ from Section 2.5 is reused to denote a vector of features extracted from \mathbf{x} ; this notation indicates that it is the solution features that are used to compute the optimal alignment via dynamic time warping.

One spatial dimension (coordinate x). The discrete density values on the one-dimensional grid are a vector $\rho \in \mathbb{R}^{n_x}$. The feature vector ζ is extracted by differentiating the density in space; on the uniform grid, the denominators of the finite difference ratios are all equal and can be scaled out. The feature vector extracted by differentiation is given in MATLAB notation as :

$$\zeta = \begin{bmatrix} 0 \\ \Delta\rho \end{bmatrix} \equiv \begin{bmatrix} 0 & \rho_2 - \rho_1 & \cdots & \rho_{n_x} - \rho_{n_x-1} \end{bmatrix}^\top \in \mathbb{R}^{n_x}, \quad (26)$$

which is the backward difference quotient, i.e., a scaled first-order backward finite difference approximation to $\frac{\partial\rho}{\partial x}$. An entry with zero value is added as the first element of ζ in eq. (26), to obtain $\zeta \in \mathbb{R}^{n_x}$ and assign a difference value to every element of the ρ sequence. This is tantamount to assuming a ghost node added to the left of the grid, with the same value ρ_1 as the first grid boundary node. The boundary element may have to be chosen differently if the boundary conditions of the specific problem necessitate it. For example, Figure 2a shows the extracted features for the densities from the example in Figure 1.

Two spatial dimensions (coordinates x and y). Next, the feature matrix for the two-dimensional (in x and y) Euler equations is obtained from the density values on the grid with $n_x \times n_y$ nodes as

$$\begin{aligned} \zeta &= \begin{bmatrix} 0 & \mathbf{0}_{n_y-1}^\top \\ \mathbf{0}_{n_x-1} & \Delta\rho \end{bmatrix} \in \mathbb{R}^{n_x \times n_y}, \quad \text{with} \\ \Delta\rho &= \left[\rho_{i,j} - \rho_{i-1,j} - (\rho_{i,j-1} - \rho_{i-1,j-1}) \right]_{2 \leq i \leq n_x, 2 \leq j \leq n_y} \in \mathbb{R}^{(n_x-1) \times (n_y-1)}. \end{aligned} \quad (27)$$

which is a scaled version of the mixed backward finite difference that approximates $\partial^2\rho/\partial x\partial y$. For brevity, we denote the finite differenced densities in both eq. (26) and section 3.1 by $\Delta\rho$.

Remark 3. Experimentally, the alignment paths behaved similarly concerning different differencing operators (forward, backward, central) in eq. (26). Second-order difference quotients of the density (similar to shadowgraph figures [48]) were also explored, which again, did not result in qualitatively superior alignment for the tested problems. Using the numerical Schlieren for feature alignment, i.e., the magnitude of the density gradient ($\zeta = |\nabla\rho|$) given in the discrete sense by

$$\zeta = \begin{bmatrix} 0 & \mathbf{0}_{n_y-1}^\top \\ \mathbf{0}_{n_x-1} & \sqrt{(\rho_{2:n_x,:} - \rho_{1:(n_x-1),:})^2 + (\rho_{2:n_x,:} - \rho_{:,1:(n_y-1)})^2} \end{bmatrix}, \quad (28)$$

performed poorly in 2D problem from section 4.5 compared to the chosen $\Delta\rho$ from section 3.1.

Remark 4 (Multiple physical variables). When features need to be extracted from multiple physical variables, for example, from both ρ and p , the feature vector ζ in one dimension (26) can be chosen as

$$\zeta = K_\rho \begin{bmatrix} 0 \\ \Delta\rho \end{bmatrix} + K_p \begin{bmatrix} 0 \\ \Delta p \end{bmatrix}, \quad (29)$$

with scaling coefficients K_ρ and K_p chosen to control the contribution of the respective terms into the feature vector.

3.2. Aligned addition convex combinations of particle states

Here, we discuss the aligned addition convex combination operation for two particles \mathbf{x} and $\hat{\mathbf{x}}$ given a general alignment path $\pi = \{(i_v, \hat{i}_v)\}_{v=1}^\ell$ (not necessarily optimal), and the mixing coefficient α (see eq. (16)). Note that all the physical variables $[\rho, \mathbf{u}, E]$ must be aligned along the same alignment path π to retain physical consistency.

We now discuss the procedure to compute feature-aware convex combinations of the density components of two particles ρ and $\hat{\rho}$.

In the 1D case, an interpolant $\mathcal{I} : \mathbb{R}^+ \rightarrow \mathbb{R}$ is constructed that maps the convex combination of the alignment indices $(i_v, \hat{i}_v) \in \pi$ to the same convex combination of the corresponding sequence element values:

$$\mathcal{I}\left(\alpha i_v + (1 - \alpha) \hat{i}_v\right) = \rho_{i_v} + (1 - \alpha) \hat{\rho}_{\hat{i}_v}, \quad v = 1, \dots, \ell. \quad (30)$$

Because i_v and \hat{i}_v are both non-decreasing with v , $\alpha i_v + (1 - \alpha) \hat{i}_v$ is also non-decreasing. The feature-aware convex combination $\bar{\rho}$ is obtained by sampling the interpolant at the points $\{v\}_{v=1}^{n_x}$, i.e.,

$$\bar{\rho} = \left[\mathcal{I}(1) \quad \mathcal{I}(2) \quad \dots \quad \mathcal{I}(n_x) \right]. \quad (31)$$

When constructing the interpolant (30) the nearest neighbor approximation [50] (where the interpolated value at the queried argument takes the value of the nearest defined argument) is preferred over other interpolation methods as it results in the least amount of feature smoothing, thereby preserving the discontinuous features better.

The procedure is similar for the 2D case, where the interpolant $\mathcal{I} : \mathbb{R}^+ \times \mathbb{R}^+ \rightarrow \mathbb{R}$ is constructed with

$$\mathcal{I}\left(\alpha i_\iota + (1 - \alpha) \hat{i}_\iota, \alpha j_\nu + (1 - \alpha) \hat{j}_\nu\right) = \alpha \rho_{i_\iota, j_\nu} + (1 - \alpha) \hat{\rho}_{\hat{i}_\iota, \hat{j}_\nu}, \quad (32)$$

where $\iota = 1, \dots, \ell_{\text{row}}$ and $\nu = 1, \dots, \ell_{\text{col}}$. The feature-aware convex combination $\bar{\rho}$ is obtained by sampling the interpolant at the (x, y) coordinates $\{(\iota, \nu)\}_{\nu=1, \iota=1}^{n_y, n_x}$ i.e.

$$\bar{\rho} = \begin{bmatrix} \mathcal{I}(1, 1) & \mathcal{I}(1, 2) & \dots & \mathcal{I}(1, n_y) \\ \mathcal{I}(2, 1) & \mathcal{I}(2, 2) & \dots & \mathcal{I}(2, n_y) \\ \vdots & \vdots & \ddots & \vdots \\ \mathcal{I}(n_x, 1) & \mathcal{I}(n_x, 2) & \dots & \mathcal{I}(n_x, n_y) \end{bmatrix}. \quad (33)$$

Feature-aware convex combinations for the other variables $\bar{\mathbf{u}}$ and \bar{E} are obtained by applying the same procedure: specific interpolants for each variable

are constructed by replacing $\rho, \hat{\rho}$ in eq. (30) with $\mathbf{u}, \hat{\mathbf{u}}$ and $\mathbf{E}, \hat{\mathbf{E}}$, respectively.

For brevity of notation, we denote the aligned convex combination of $\rho, \hat{\rho}$ (in both 1D and 2D) for a given alignment path π and mixing coefficient α by:

$$\bar{\rho} =: \rho \oplus_{\alpha, \pi} \hat{\rho}. \quad (34)$$

With the above notation, the aligned convex combination of two particle states \mathbf{x} and $\hat{\mathbf{x}}$ is:

$$\bar{\mathbf{x}} = \mathbf{x} \oplus_{\alpha, \pi} \hat{\mathbf{x}} = \begin{bmatrix} \rho \\ \mathbf{u} \\ E \end{bmatrix} \oplus_{\alpha, \pi} \begin{bmatrix} \hat{\rho} \\ \hat{\mathbf{u}} \\ \hat{E} \end{bmatrix} := \begin{bmatrix} \rho \oplus_{\alpha, \pi} \hat{\rho} \\ \mathbf{u} \oplus_{\alpha, \pi} \hat{\mathbf{u}} \\ E \oplus_{\alpha, \pi} \hat{E} \end{bmatrix} = \begin{bmatrix} \bar{\rho} \\ \bar{\mathbf{u}} \\ \bar{E} \end{bmatrix}. \quad (35)$$

In summary, computing the optimal aligned convex combination of two particles \mathbf{x} and $\hat{\mathbf{x}}$ for a given α (where $0 \leq \alpha \leq 1$) consists of the following steps:

- (i) Extract the features $\zeta, \hat{\zeta}$ for each particle using formulas (26), (27), or (29).
- (ii) Calculate the optimal alignment path π^* of the features ζ and $\hat{\zeta}$ by applying the dynamic time warping method eq. (20), with the respective distance function (eq. (19) or eqs. (22) and (23)).
- (iii) Compute the feature aligned convex combination $\mathbf{x} \oplus_{\alpha, \pi^*} \hat{\mathbf{x}}$ via eq. (35).

Example 1. *Figure 2a shows the extracted density features for the 1D example in Figure 1. Optimal feature alignment is computed using DTW, and the optimal alignment path is used to align the density fields as shown in Figure 2b. The aligned density results for different α values are shown in Figure 1b.*

3.3. The Feature-preserving ETPF

We have seen in Section 2.4 that classic ETPF is not well suited for data assimilation when the underlying system solution develops features: convex state

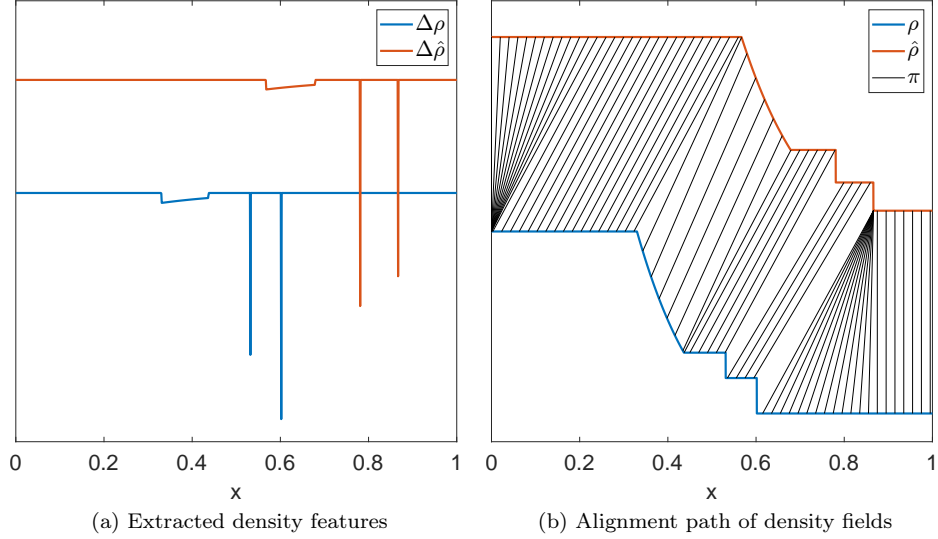


Figure 2: The left panel shows the extracted features from the fields $\rho, \hat{\rho}$ of Figure 1b. Applying DTW on the extracted features gives the optimal alignment path. The right panel shows how this path is used to align the density fields in a pointwise fashion.

combinations required by ETPF analysis smear out physical features, leading to non-physical analyses. To correct for this pitfall, we extend ETPF to account for solution features.

ETPF computes the equally weighted analysis particle states using eq. (14):

$$\mathbf{x}^{a[e]} = \mathbf{T}_{1,e} \mathbf{x}^{f[1]} + \mathbf{T}_{2,e} \mathbf{x}^{f[2]} + \dots + \mathbf{T}_{n_e,e} \mathbf{x}^{f[n_e]}, \quad e \in \{1, 2, \dots, n_e\}. \quad (36)$$

Directly replacing the standard convex combination in (36) with an aligned n_e -way convex combination requires a memory-inefficient multisequence alignment. A more effective approach is to reformulate the n_e -way convex combination in

eq. (36) as a sequence of 2-way convex combinations as follows:

$$\begin{aligned}
\tilde{\mathbf{x}}^{\text{f}[2,e]} &= \alpha_1^{[e]} \mathbf{x}^{\text{f}[1]} + (1 - \alpha_1^{[e]}) \mathbf{x}^{\text{f}[2]}, \\
\tilde{\mathbf{x}}^{\text{f}[3,e]} &= \alpha_2^{[e]} \tilde{\mathbf{x}}^{\text{f}[2,e]} + (1 - \alpha_2^{[e]}) \mathbf{x}^{\text{f}[3]}, \\
&\vdots \\
\mathbf{x}^{\text{a}[e]} &\equiv \tilde{\mathbf{x}}^{\text{f}[n_e,e]} = \alpha_{n_e-1}^{[e]} \tilde{\mathbf{x}}^{\text{f}[n_e-1,e]} + (1 - \alpha_{n_e-1}^{[e]}) \mathbf{x}^{\text{f}[n_e]}.
\end{aligned} \tag{37}$$

The α coefficients are obtained by equating eq. (36) with eq. (37) giving

$$\alpha_v^{[e]} = \frac{\sum_{i=1}^v \mathbf{T}_{i,e}}{\sum_{i=1}^{v+1} \mathbf{T}_{i,e}} \text{ for all } v \in \{1, 2, \dots, n_e - 1\}, \quad 0 < \alpha_v^{[e]} < 1. \tag{38}$$

Replacing the two-way convex combinations in eq. (37) with the corresponding optimally aligned two-way convex combinations gives the aligned n_e -way convex combination:

$$\begin{aligned}
\tilde{\mathbf{x}}^{\text{f}[2,e]} &= \alpha_1^{[e]} \mathbf{x}^{\text{f}[1]} \oplus_{\alpha_1^{[e]}, \pi_1^*} (1 - \alpha_1^{[e]}) \mathbf{x}^{\text{f}[2]}, \\
\tilde{\mathbf{x}}^{\text{f}[3,e]} &= \alpha_2^{[e]} \tilde{\mathbf{x}}^{\text{f}[2,e]} \oplus_{\alpha_2^{[e]}, \pi_2^*} (1 - \alpha_2^{[e]}) \mathbf{x}^{\text{f}[3]}, \\
&\vdots \\
\mathbf{x}^{\text{a}[e]} &= \alpha_{n_e-1}^{[e]} \tilde{\mathbf{x}}^{\text{f}[n_e-1,e]} \oplus_{\alpha_{n_e-1}^{[e]}, \pi_{n_e-1}^*} (1 - \alpha_{n_e-1}^{[e]}) \mathbf{x}^{\text{f}[n_e]},
\end{aligned} \tag{39}$$

where π_j^* is the optimal alignment path for $\tilde{\mathbf{x}}^{\text{f}[j,e]}$ and $\mathbf{x}^{\text{f}[j+1]}$.

Repeating eq. (39) for all $e \in \{1, 2, \dots, n_e\}$ results in the feature-preserving ETPF.

Remark 5 (Computational cost). *Each aligned n_e -way convex combination (39) requires $(n_e - 1)$ runs of the DTW alignment algorithm. The feature-preserving ETPF requires n_e aligned convex combinations, therefore, the total cost includes $n_e(n_e - 1)$ DTW alignment algorithm runs.*

Remark 6. *One may ask if the ETPF distance matrix \mathbf{D} computation in Algorithm 1 should now use the optimal warping distance from eq. (20) rather*

than the 2-norm. While this approach is theoretically consistent with (39), it is more expensive as computing all pairwise particle distances requires an additional $n_e(n_e - 1)/2$ DTW runs. Additionally, the optimal warped distance based on the DTW is not a true metric as it violates the triangle inequality. The authors recommend using the 2-norm as no benefit has been observed from incorporating the warped distance into the ETPF distance matrix.

4. Numerical experiments

We test the feature-preserving ETPF formulation on four different test cases, namely (i) the 1D Sod’s shock tube [36], (ii) the 1D Toro’s shock tube [5], (iii) the 1D Shu-Osher shock-entropy interaction [51], and (iv) a 2D blast wave. The standard ETPF and the feature-preserving ETPF are compared on (i) the quality of preserved features for each problem, and (ii) the relative average ensemble error given by

$$\text{Error}(t_k) = \frac{\sum_{e=1}^{n_e} \|\mathbf{x}_k^{\text{true}} \mathbf{1}^\top - \mathbf{x}_k^{\text{a}[e]}\|_2}{n_e \|\mathbf{x}_k^{\text{true}}\|} \quad (40)$$

We look at the space-time plots of density and entropy and compare the truth (reference solution) with the computed analysis. The physical units are: (i) m for length, (ii) kg m^{-3} for density (ρ), (iii) m s^{-1} for velocity (\mathbf{u}), (iv) J m^{-3} for energy density (E), (v) Pa for pressure (p) and (vi) J (kg K)^{-1} for entropy (s). For the remainder of this section, the units of measurement are omitted for brevity.

Model Settings. The Euler equations use the WENO5 [52] finite difference spatial discretization with a Lax-Friedrichs flux limiter and a third-order total variation diminishing Runge-Kutta [53] for time stepping. There is no inflow in the problem, as flow is driven by the initial pressure, density, and velocity variations. All problem setups have outflow boundary conditions at every boundary, ensuring there are no boundary interactions. The adiabatic index for all experiments is $\gamma = 1.4$.

The 1D experiments are discretized on the domain $[0, 1]$ using 5001 grid points, and the 2D experiment is discretized on $[0, 2] \times [0, 2]$ domain on a 401×401 uniform grid. The temporal discretization differs for each test case and is specified in the corresponding subsections.

All experiments are run on MATLAB 2024b. Our simulation code was adapted from the repository of Manuel A. Diaz [54].

Observation settings. In this work, it is assumed that: (i) the observation operators do not change with time, i.e., $\tilde{\mathcal{H}}_k = \tilde{\mathcal{H}}$ and $\mathcal{H}_k = \mathcal{H}$, $\forall k$ (see eqs. (4) and (6)); and (ii) the statistics of the observation error density are known and not changing in time, i.e., $\epsilon_k \sim \mathcal{P}^\circ$. The observation errors are normally distributed as $\mathcal{P}^\circ = \text{Normal}(\mathbf{0}, \mathbf{R})$ with $\mathbf{R} = 0.1\mathbf{I}$.

- For all the 1D experiments, pressure is observed at 9 different locations: $\{0.1, 0.2, \dots, 0.9\}$ inside the shock tube (see Figure 3g). This results in a non-linear observation for the particles as the pressure is computed from the equation of state (see eq. (2)).
- For the 2D blast wave, we observe the pressure at 81 locations, on a 9×9 2D grid $\{0.2, 0.4, \dots, 1.8\} \times \{0.2, 0.4, \dots, 1.8\}$ (locations marked in Figure 14a).

Filtering settings. All problems employ $n_e = 20$ particles. The initial particles are parametrically sampled from a normal distribution around the true parameters with a given standard deviation. For example, let the true state in the 1D problem (where a diaphragm at x_d^{true} divides a shock tube into two regions) be described as

$$(\rho^{\text{true}}, u^{\text{true}}, p^{\text{true}}) = \begin{cases} (\rho_L^{\text{true}}, u_L^{\text{true}}, p_L^{\text{true}}) & 0 \leq x \leq x_d^{\text{true}}, \\ (\rho_R^{\text{true}}, u_R^{\text{true}}, p_R^{\text{true}}) & x_d^{\text{true}} \leq x \leq 1. \end{cases} \quad (41)$$

The true pressure in the left region is given by p_L^{true} , and each particle in the initial ensemble draws the pressure in the left region (constant across $0 \leq x \leq x_d$) as

$$p_L^{[e]} \sim \text{Normal}(p_L^{\text{true}}, \sigma(p_L)) \quad \text{for all } e \in \{1, \dots, n_e\}, \quad (42)$$

where $\sigma(p_L)$ is the initial standard deviation. Other variables such as $\rho_L, u_L, \rho_R, u_R, p_R$ and x_d are drawn similarly from a normal distribution around the initial true state and a given standard deviation. For a fair comparison, the initial ensemble and the observation trajectory (over time) are identical for both the ETPF and feature-preserving ETPF.

Both filters (standard ETPF and feature-preserving ETPF) are applied to the discrete forecast ensemble given by $\mathbf{x}_k^{\text{f}[e]} = [\rho_k^{\text{f}[e]}, \mathbf{u}_k^{\text{f}[e]}, E_k^{\text{f}[e]}]$ for all $e \in \{1, \dots, n_e\}$ at every time step t_k . To deal with the weight degeneracy problem [11], we underweigh the particles in the likelihood weight computation (for both the ETPF and feature-preserving ETPF) by scaling the observation error covariance with a scalar $\beta_w \mathbf{R}$ (as proposed by Zanetti et. al. [55]). This also alleviates the need to add stochastic noise, called rejuvenation [17], to keep the particles different.

4.1. 1D problem: Sod's shock tube

This setup follows that of Gary A. Sod [36]. The test case consists of a rarefaction wave that moves to the left, a contact discontinuity, and a shockwave, both moving to the right. The initial condition for \mathbf{x}^{true} is described by

$$(\rho^{\text{true}}, u^{\text{true}}, p^{\text{true}}) = \begin{cases} (1, 0, 1) & 0 \leq x \leq 0.5, \\ (0.125, 0, 0.1) & 0.5 \leq x \leq 1, \end{cases} \quad (43)$$

where a diaphragm at $x_d^{\text{true}} = 0.5$ separates the two regions of gas.

The initial ensemble is drawn around the true state with the following standard deviations $\sigma(\rho_L) = 0.05, \sigma(\rho_R) = 0.006, \sigma(p_L) = 0.05, \sigma(p_R) = 0.005$ and $\sigma(x_d) = 0.2$ (see eqs. (41) and (42) and its discussion for more details). The model is run from $t = 0$ until $t = 0.2$, with observations coming in every $\Delta t = \frac{0.2}{100}$. To allow the features to develop, no assimilation is performed for the initial 10 steps (until $t = 0.02$). The underweighting constant for the observation error covariance is set as $\beta_w = 20$. Numerical results are reported in Figures 3 to 6.

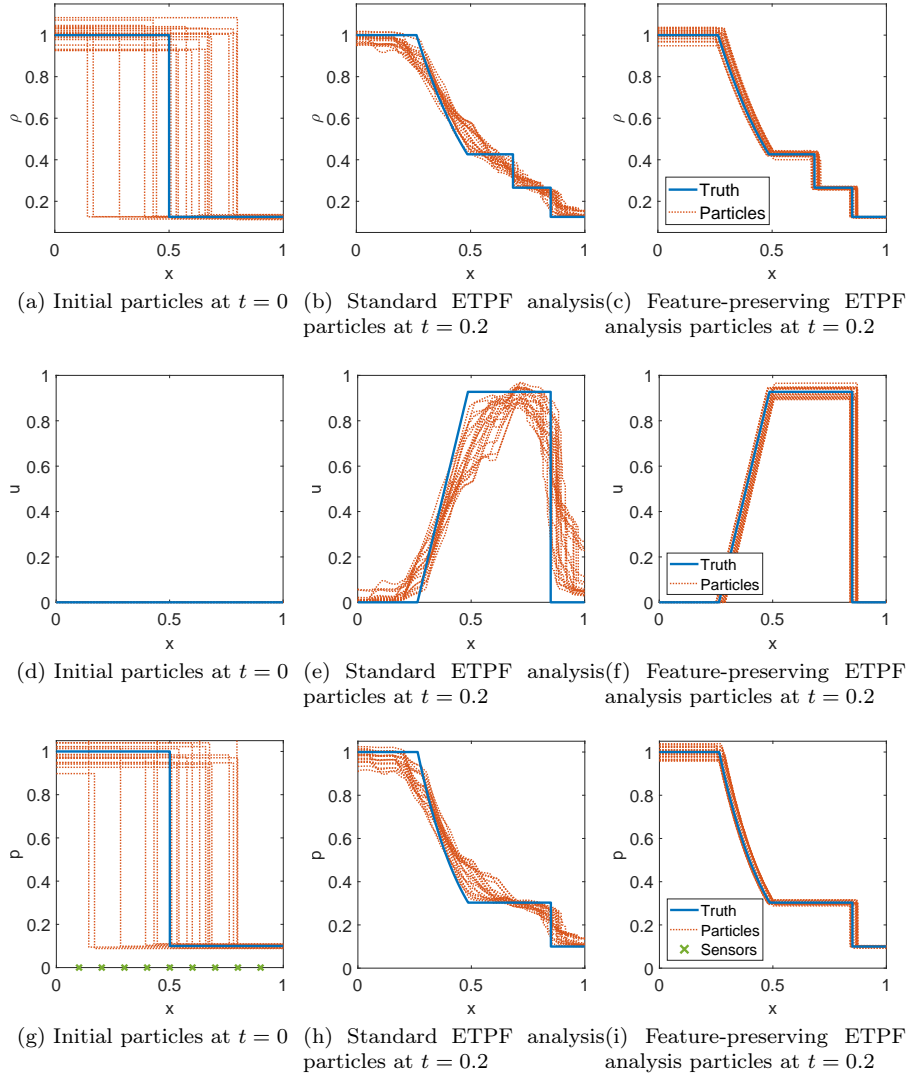
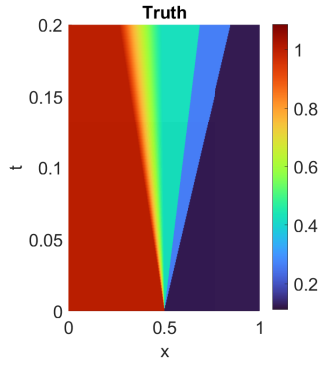
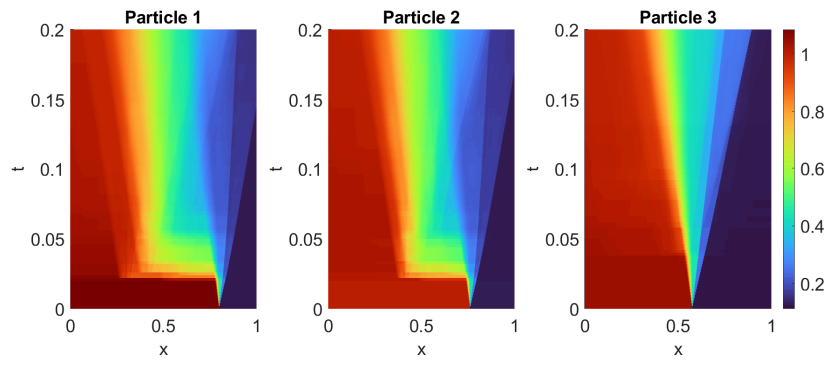


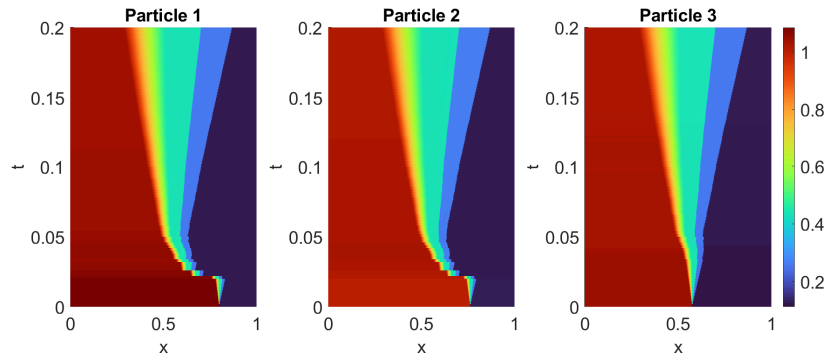
Figure 3: Density (top row), velocity (middle row), and pressure (bottom row) snapshots for Sod's shock tube problem (eq. (43)). The observation sensor locations are shown in the leftmost pressure subplot.



(a) Reference truth



(b) Standard ETPF analysis



(c) Feature-preserving ETPF analysis

Figure 4: Spacetime evolution of density for Sod's shock tube problem (eq. (43)).

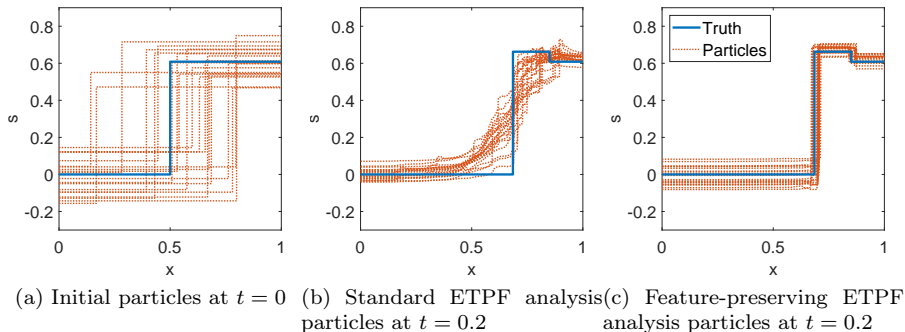


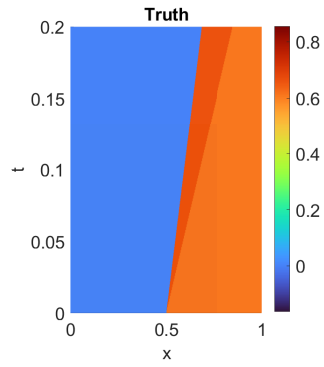
Figure 5: Entropy snapshots for Sod’s shock tube problem (eq. (43)).

First, we look at the densities in Figures 3 and 4. Figure 3a shows the initial setup of the problem. Figures 3b and 3c show the analysis densities at the final time for each filter. While the standard ETPF tracks the density, the features are lost as in Figure 3b. However, the feature-preserving ETPF in Figure 3b preserves each feature—the shockwave, the rarefaction wave, and the contact discontinuity—while also tracking the density correctly.

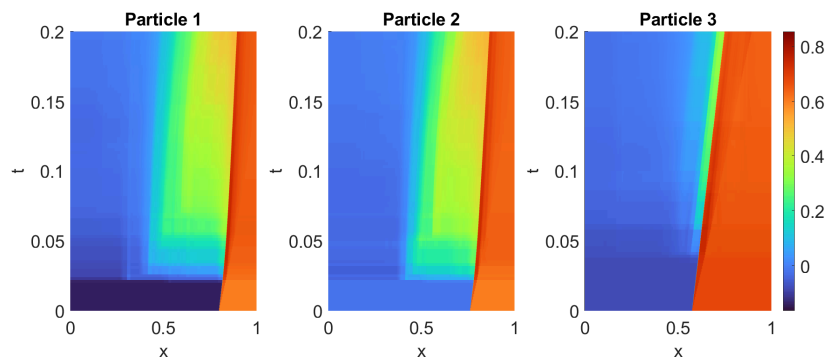
The velocity (see Figures 3d to 3f) and pressure (see Figures 3g to 3i) solutions behave similarly: the feature-preserving ETPF preserves the features when the standard ETPF fails.

Figure 4 shows the evolution of the density and the features in space-time for the reference truth (Figure 4a) and 3 particles out of the 20 (the same three particles are shown for both the ETPF and the feature-preserving ETPF). As seen in Figure 4a, there are five distinct density regions in Sod’s shock tube. The space-time plot for the standard ETPF (see Figure 4b) shows *feature smearing* over time, and the five distinct regions are not sharply distinct anymore. However, the space-time plot for the feature-preserving ETPF (see Figure 4c) shows the five distinct solution regions.

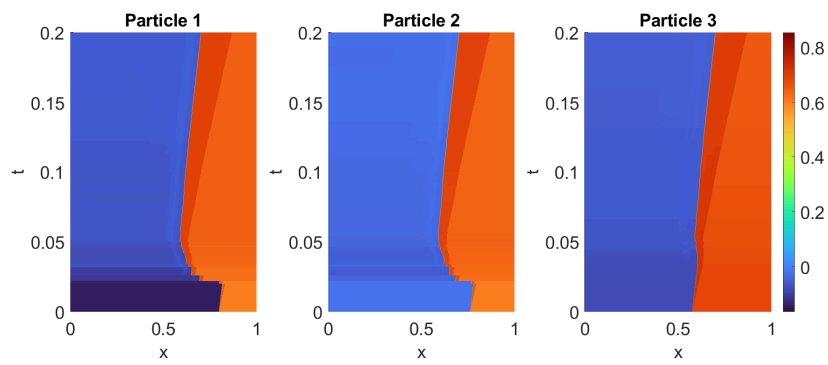
Next, we look at the entropy (see eq. (3)) results in Figures 5 and 6; entropy is a quantity of interest not computed directly, but derived from the primary variables. Figure 5a shows the initial setup of the assimilation problem. Figures 5b and 5c show the analysis entropies at the final time for both filters. The



(a) Reference truth



(b) Standard ETPF analysis



(c) Feature-preserving ETPF analysis

Figure 6: Spacetime evolution of entropy for Sod's shock tube problem (eq. (43)).

feature-preserving ETPF in Figure 5c captures the entropy correctly as well. As the truth shows in Figure 6a, the entropy has three distinct regions—between the left boundary and the contact discontinuity, between the constant discontinuity and the shockwave, and between the shockwave and the left boundary. The distinct entropy regions are lost for the standard ETPF as shown in Figure 6b. However, the feature-preserving ETPF in Figure 6c captures the three distinct entropy regions.

4.2. 1D problem: Toro’s shock tube

This setup follows test case 4 from E.F. Toro [5]. This problem consists of three discontinuities moving towards the right end of the tube. The initial condition for \mathbf{x}^{true} is described by

$$(\rho^{\text{true}}, u^{\text{true}}, p^{\text{true}}) = \begin{cases} (5.99924, 19.5975, 460.894) & 0 \leq x \leq x_d^{\text{true}}, \\ (5.99242, -6.19633, 46.0950) & x_d^{\text{true}} \leq x \leq 1, \end{cases} \quad (44)$$

where a diaphragm at $x_d^{\text{true}} = 0.5$ separates the two regions of gas.

The initial ensemble is drawn as described in eqs. (41) and (42) with the standard deviations $\sigma(\rho_L) = 0.2, \sigma(\rho_R) = 0, \sigma(p_L) = 10, \sigma(p_R) = 1$ and $\sigma(x_d) = 0.1$. The model is evaluated from from $t = 0$ until $t = 0.0245$, with observations coming in every $\Delta t = \frac{0.0245}{70}$. No assimilation is done for the initial 10 steps, to allow the features to develop. The underweighting constant for the observation error covariance is set to $\beta_w = 10^8$. While this is quite large, it is successful in practice as the experiments show, and is necessary to account for the scaling of the observations. The results are reported in Figures 7 to 10.

First, we consider the densities in Figures 7 and 8. Figure 7a depicts the problem setup. While the density variations are small, the entropy variations (caused by large pressure variance) are large enough to be seen in Figure 9a. Figures 7b and 7c show the analysis densities at the final time. As before, the standard ETPF loses track of the features, resulting in highly spurious densities (see Figure 7b). However, the feature-preserving ETPF in Figure 7b

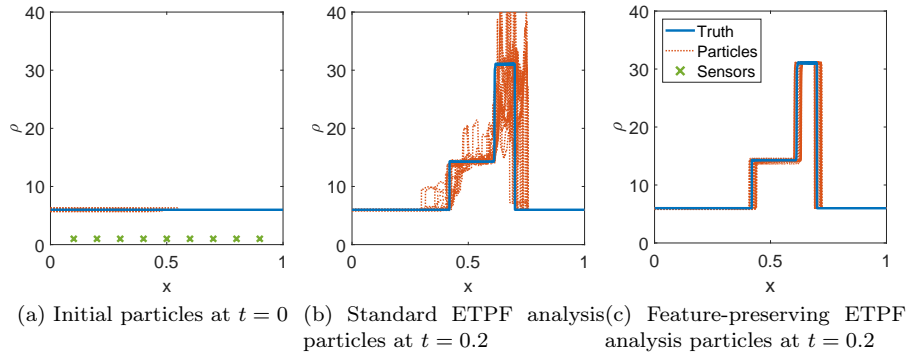
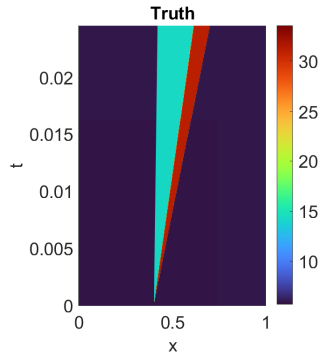


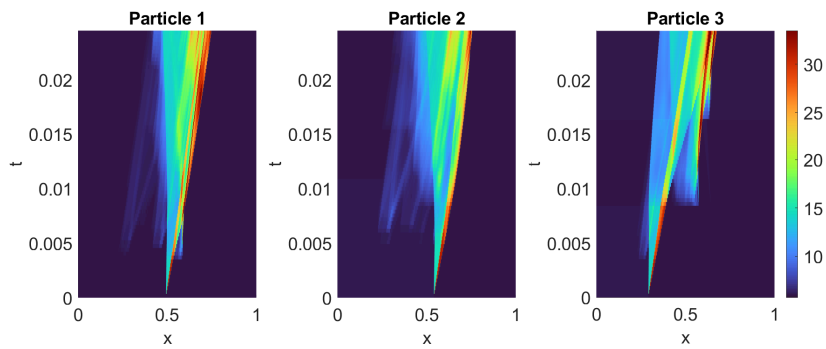
Figure 7: Density snapshots for Toro’s shock tube problem (eq. (44)). The locations of the pressure sensors are shown in Figure 7a.

preserves each feature—the three discontinuities—while also tracking the density correctly. Figure 8 shows the evolution of the density and the features in space and time for the reference truth (Figure 8a) and three particles out of the twenty. As seen in Figure 8a, there are 4 distinct density regions in Toro’s shock tube. As previously seen, the spacetime plot for the standard ETPF (see Figure 8b) shows feature smearing over time. However, the spacetime plot for the feature-preserving ETPF (see Figure 8c) preserves the four distinct regions.

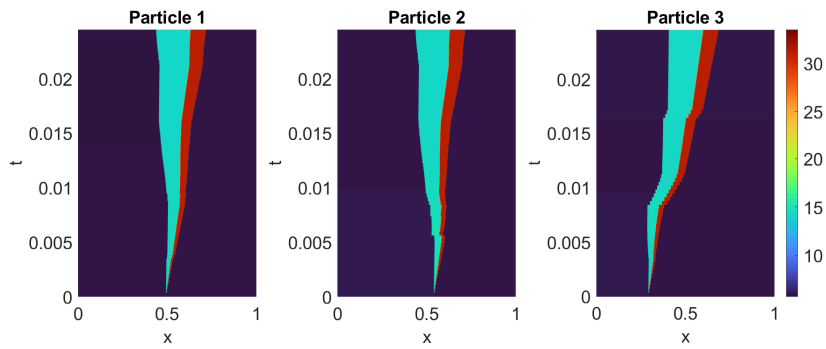
Next, we look at the entropy (see eq. (3)) in Figures 9 and 10 for this problem. Figure 9a shows the initial setup of the assimilation problem. Figures 9b and 9c show the analysis entropies at the final time for both filters. The feature-preserving ETPF in Figure 9c captures the entropy for this problem too. As the truth shows in Figure 10a, the entropy has four distinct regions all of which are smeared for the standard ETPF (see Figure 10b). However, the feature-preserving ETPF in Figure 10c captures the four distinct entropy regions correctly.



(a) Reference truth



(b) Standard ETPF analysis



(c) Feature-preserving ETPF analysis

Figure 8: Spacetime evolution of density for Toro's shock tube problem (eq. (44)).

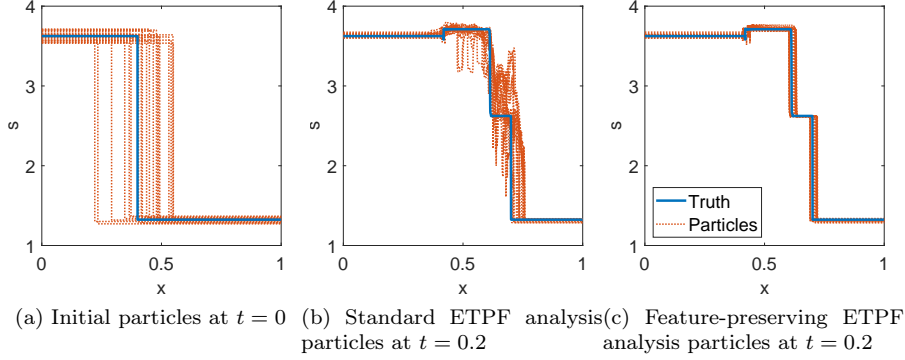


Figure 9: Entropy snapshots for Toro's shock tube problem (eq. (44)).

4.3. 1D problem: Shu-Osher shock-entropy interaction

This setup is adapted from example 6 in [51] and consists of a shockwave interacting with an entropy wave. The initial condition for \mathbf{x}^{true} is described by

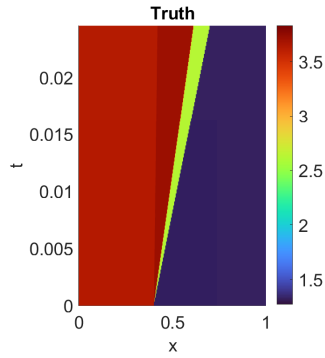
$$(\rho^{\text{true}}, u^{\text{true}}, p^{\text{true}}) = \begin{cases} (3.857143, 2.629369, 10.3333) & 0 \leq x \leq x_d^{\text{true}}, \\ (1 + 0.2 \sin(10\pi(x - x_d)), 0, 1) & x_d^{\text{true}} \leq x \leq 1, \end{cases} \quad (45)$$

where a diaphragm at $x_d^{\text{true}} = 0.1$ separates the two regions of gas. We do not report the entropy for this problem since it looks similar to the density plot.

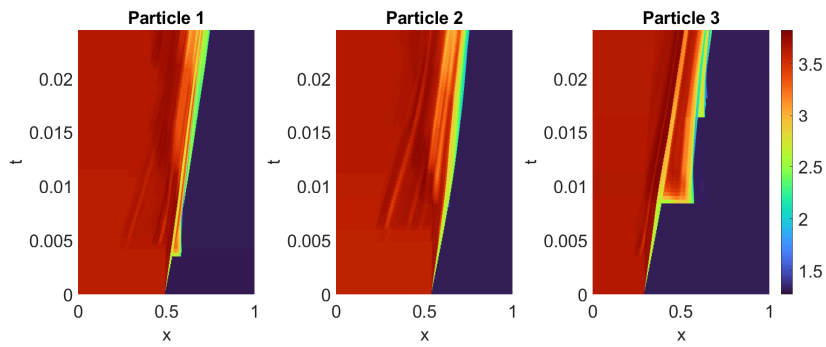
As before, we assume uncertainties about the diaphragm position, the pressure, and the density at the initial time. The initial ensemble is drawn as described in eqs. (41) and (42) with the standard deviations with the standard deviations $\sigma(\rho_L) = 0.4, \sigma(\rho_R) = 0.1, \sigma(u_L) = 0.2, \sigma(p_L) = 1.03, \sigma(p_R) = 0.1$ and $\sigma(x_d) = 0.05$.

The model is evolved from $t = 0$ until $t = 0.25$, with observations coming in every $\Delta t = \frac{0.25}{100}$. No assimilation is done for the initial 10 steps, to allow for the features to develop. The underweighting constant for the observation error covariance is set to $\beta_w = 10^3$. Note that if one assumes a different number of waves in the ensemble, the profiles do not align, causing the aligned filter to fail.

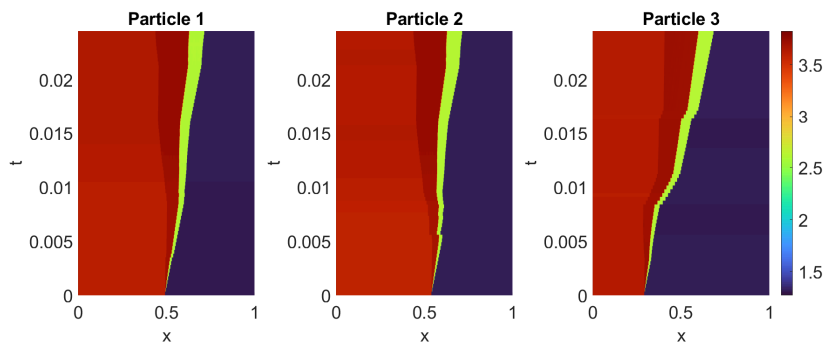
We show the densities Figures 11 and 12. Figure 11a depicts the starting problem setup. Figures 11b and 11c show the analysis densities at the final



(a) Reference truth



(b) Standard ETPF analysis



(c) Feature-preserving ETPF analysis

Figure 10: Spacetime evolution of entropy for Toro's shock tube problem (eq. (44)).

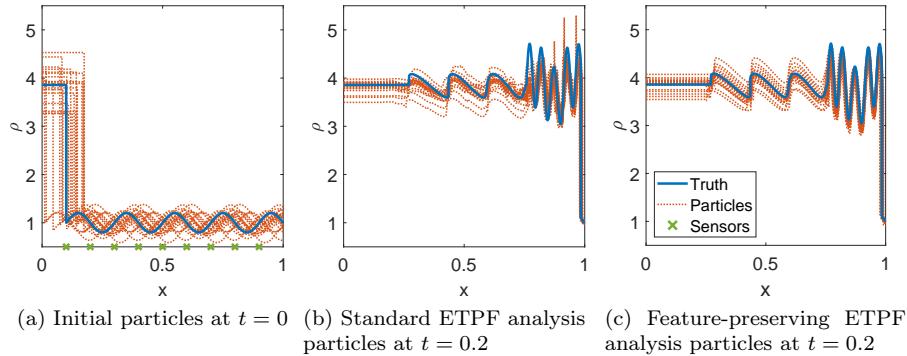
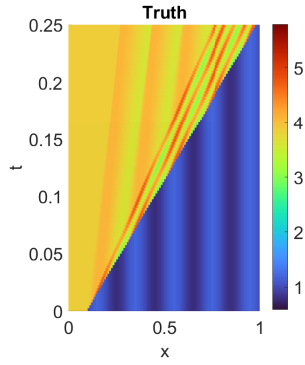


Figure 11: Density snapshots for Shu-Osher’s shock-entropy problem (eq. (45)). The locations of the pressure sensors are shown in Figure 11a.

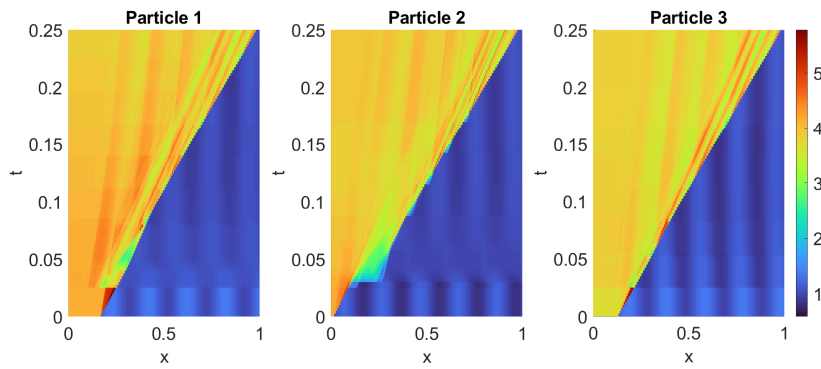
time. While the standard ETPF exhibits feature smearing, it is to a much smaller degree when compared to the previous problems (see Figure 11b). This is likely because some features—sine waves for this problem—are not sharp. However, the feature-preserving ETPF is still useful as it preserves the shapes of each wave better than plain ETPF (see Figure 11b). Figure 12 shows the evolution of the density and the features in space and time for the reference truth (Figure 12a) and three particles out of the twenty. The feature smearing for the standard ETPF is evident in the region where the shockwave and the entropy wave interact, as seen in Figure 12b. However, the smearing does not happen with the feature-preserving ETPF (see Figure 12c).

4.4. 1D problems: Assessment of analysis error

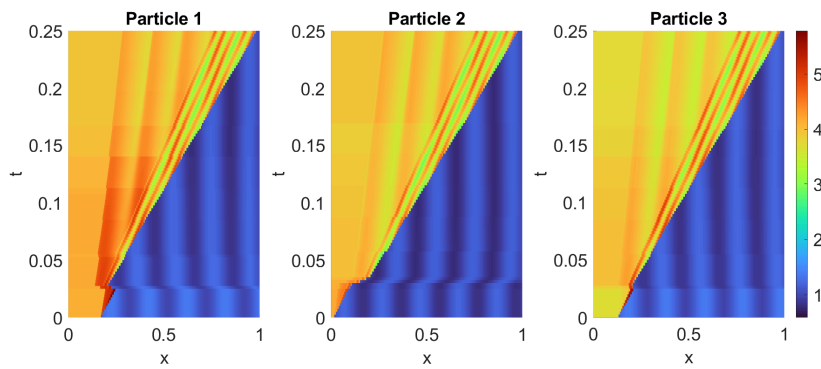
Traditionally, the quality of assimilation is measured via a spatio-temporal root mean squared error [1] between the mean analysis state and the true state, while ignoring the qualitative aspects of the state. We now compare the performance of the filters similarly using the relative average ensemble error at each time instance given in eq. (40). While this is atypical, it is more informative about the spatial error for particle filters, where each particle is assumed to be a possible estimate of the truth (rather than the particle mean being the best estimate of the truth).



(a) Reference truth



(b) Standard ETPF analysis



(c) Feature-preserving ETPF analysis

Figure 12: Spacetime evolution of density for Shu-Osher's shock-entropy problem (eq. (45)).

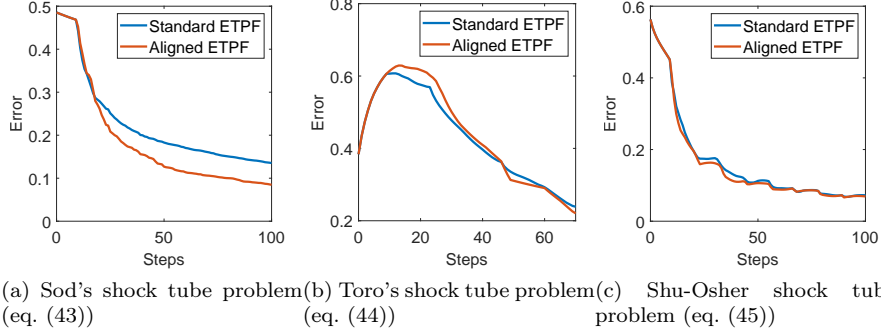


Figure 13: Relative average ensemble error for the different test problems.

Figure 13 shows the relative average ensemble error at each time step t_k for the three test problems. In the Sod's shock tube experiment (eq. (43)), both methods have the same error until step 10 as no filtering is done. Then, the feature-preserving ETPF has a slightly higher error until about step 20, after which the feature-preserving ETPF does much better than the standard ETPF. This might be occurring because the loss of features results in very different model dynamics. For Toro's shock tube (eq. (44)) and the Shu-Osher problem (eq. (45)), the standard ETPF and feature-preserving ETPF show unremarkable error results in Figure 13b, and Figure 13c respectively. Toro's shock tube could be showing worse relative error results because the errors around the discontinuities will be drastic with feature preservation, but smoothed out with the standard ETPF.

In summary, feature-preserving ETPF (and the feature-preserving filters in general) yields a similar relative average ensemble error to the standard ETPF; alignment does not lead to a degradation of analysis accuracy in the traditional sense. However, the feature-preserving ETPF gives a qualitatively superior analysis, with individual analysis particles that respect the physical behavior of the system.

4.5. 2D problem: Blast wave

In this experiment, we set a blast wave on the domain $\Omega = [0, 2] \times [0, 2]$ with initial conditions inspired by the test case of the two interacting blast waves in 1D [56]. The problem is set up as

$$(\rho^{\text{true}}, \mathbf{u}^{\text{true}}, p^{\text{true}}) = \begin{cases} (\rho_{\Omega_1}^{\text{true}}, \mathbf{u}_{\Omega_1}^{\text{true}}, p_{\Omega_1}^{\text{true}}) & (x, y) \in \Omega_1, \\ (\rho_{\Omega_2}^{\text{true}}, \mathbf{u}_{\Omega_2}^{\text{true}}, p_{\Omega_2}^{\text{true}}) & (x, y) \in \Omega_2. \end{cases} \quad (46)$$

having different ρ, \mathbf{u}, p in two regions: Ω_1 as the circular region containing the blast wave; and the exterior (of the blast wave) region $\Omega_2 = \Omega \setminus \Omega_1$. Here, \mathbf{u} refers to the velocities in the x and y directions. At the initial time, \mathbf{x}^{true} is described by

$$(\rho^{\text{true}}, \mathbf{u}^{\text{true}}, p^{\text{true}}) = \begin{cases} (1, \mathbf{0}, 1000) & (x, y) \in \Omega_1, \\ (1, \mathbf{0}, 0.01) & (x, y) \in \Omega_2, \end{cases} \quad (47)$$

with the center of the blast wave $(x_c^{\text{true}}, y_c^{\text{true}}) = (1, 1)$ with radius $r^{\text{true}} = 0.4$.

We assume uncertainties about the blast wave's radius and location (of its center), along with the density and pressure in Ω_1 . The initial ensemble is drawn as $x_c^{[e]} \sim \text{Normal}(x_c^{\text{true}}, \sigma(x_c))$, $y_c^{[e]} \sim \text{Normal}(y_c^{\text{true}}, \sigma(y_c))$, $r^{[e]} \sim \text{Normal}(r^{\text{true}}, \sigma(r))$, $\rho_{\Omega_1}^{[e]} \sim \text{Normal}(\rho_{\Omega_1}^{\text{true}}, \sigma(\rho_{\Omega_1}))$, and $p_{\Omega_1}^{[e]} \sim \text{Normal}(p_{\Omega_1}^{\text{true}}, \sigma(p_{\Omega_1}))$ for all $e \in \{1, \dots, n_e\}$, where the standard deviations $\sigma(x_c) = \sigma(y_c) = 0.2$, $\sigma(r) = 0.05$, $\sigma(\rho_{\Omega_1}) = 0.05$ and $\sigma(p_{\Omega_1}) = 0.1$. The model is evaluated from from $t = 0$ until $t = 0.01$, with observations coming in every $\Delta t = \frac{0.01}{100}$. Assimilation is done after the first 10 steps to allow for the features to develop. The underweighting constant for the observation error covariance is $\beta_w = 10^7$.

Figure 14 shows the true density (see Figure 14a) and three different background particle densities (see Figure 14b) at the initial time. The initial background particles are identical across the standard ETPF and feature-preserving ETPF methods. Similarly, Figure 15 shows the true pressure (see Figure 15a) and three different background particle pressures (see Figure 15b). Figure 16a

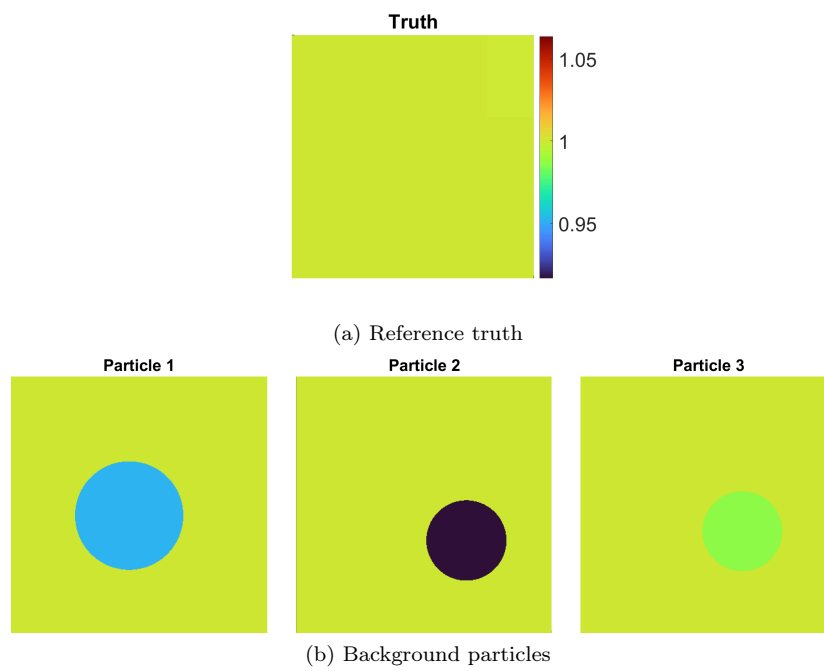


Figure 14: Density snapshot at $t = 0$. The background particles are common to both ETPF and feature-preserving ETPF. Note that density is constant for the truth.

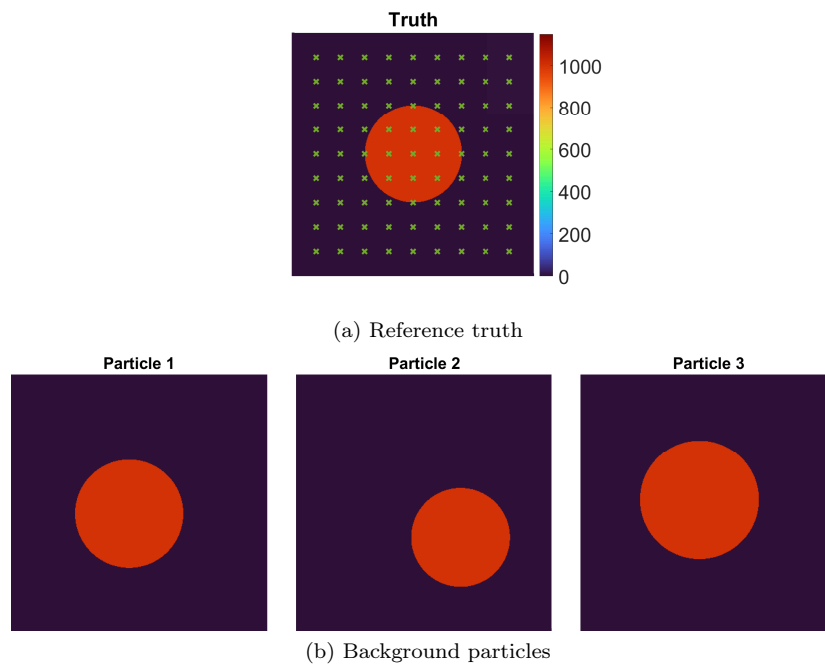


Figure 15: Pressure snapshot at $t = 0$. The background particles are common to both ETPF and feature-preserving ETPF. Also shown with the reference truth are the locations of the pressure sensors, marked by the \times .

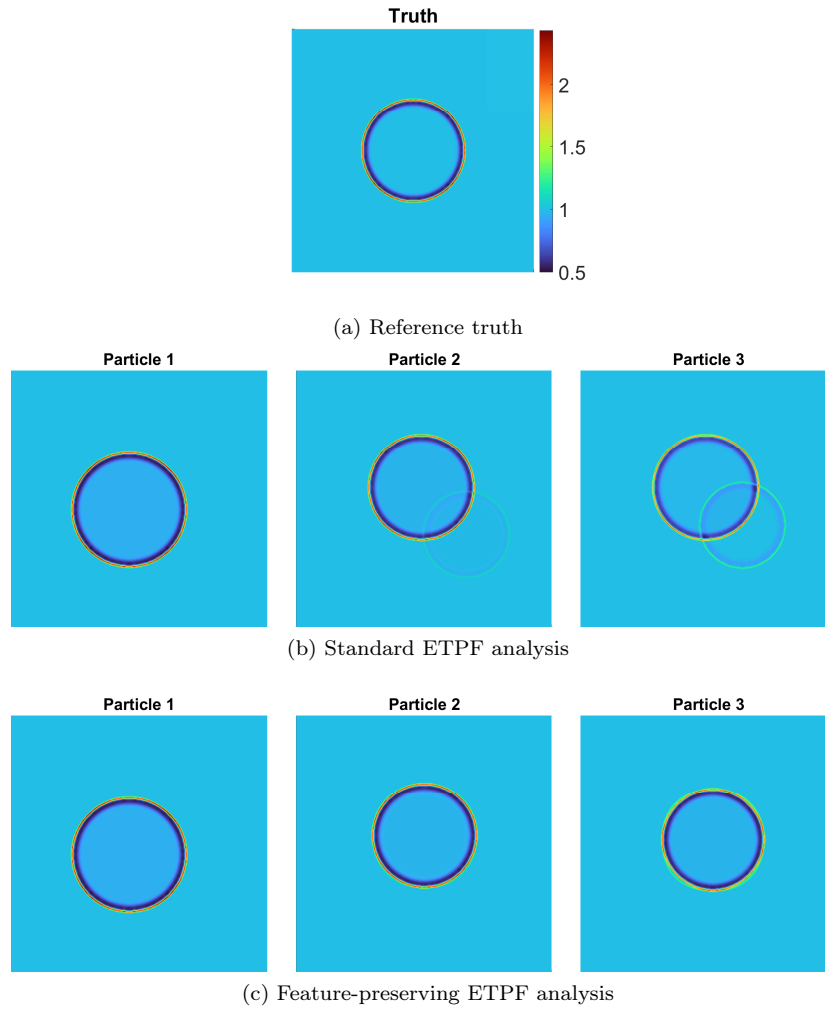


Figure 16: Density snapshots at $t = 0.001$ after one (1) assimilation cycle.

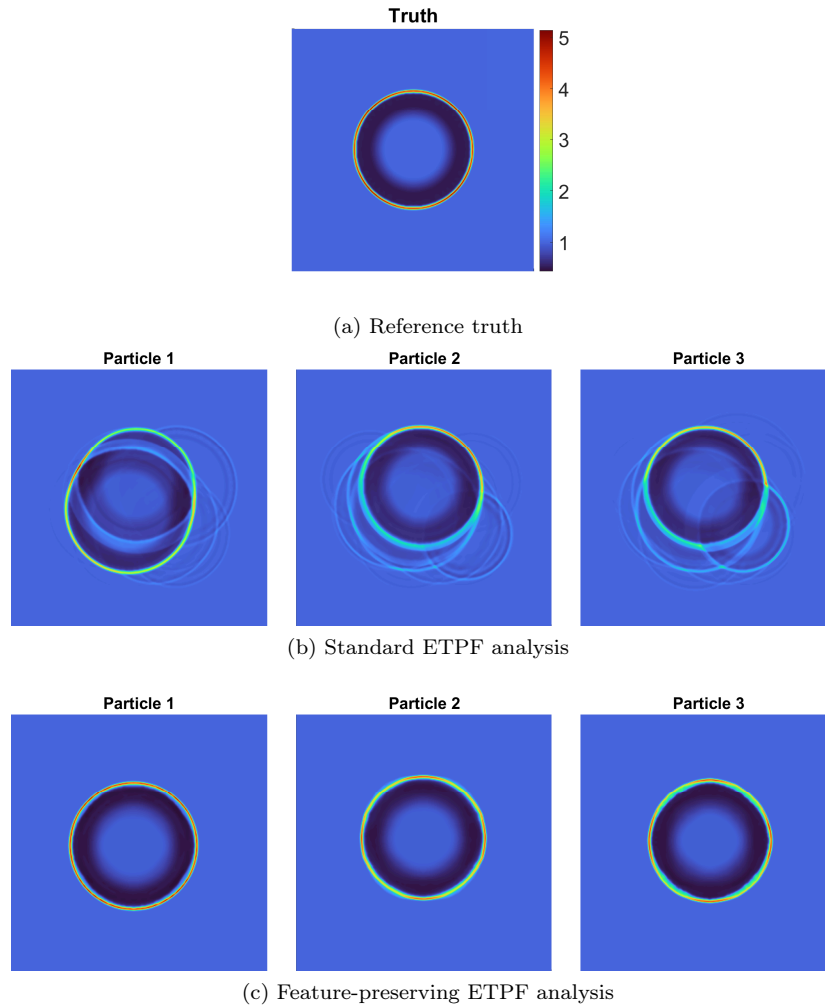


Figure 17: Density snapshot at $t = 0.004$ after 30 assimilation cycles.

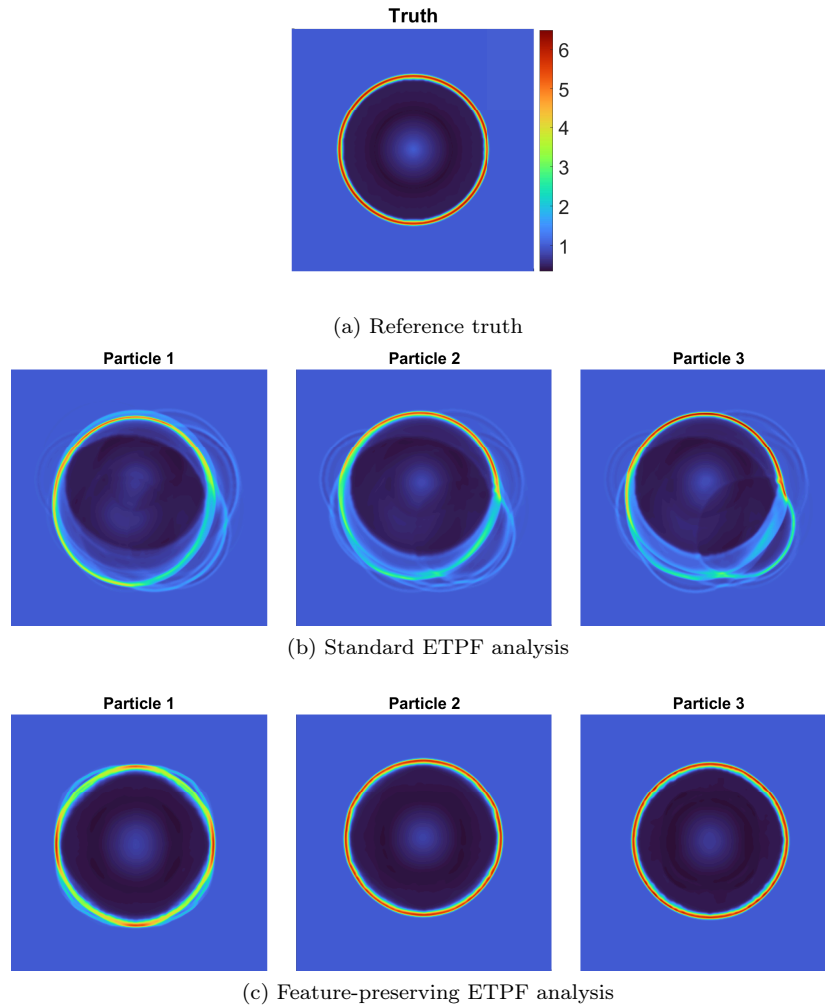


Figure 18: Density snapshot at $t = 0.01$ after 90 assimilation cycles.

shows the true (reference) solution at the first assimilation step $t = 0.001$. From Figure 16b, we see that the standard ETPF analysis particles 2 and 3 have already lost the distinct wavefront structure and have multiple rings in the state. The wavefront structure is retained by particle 1 because it has a dominant weight and has not been combined with any other particle. However, as seen in Figure 16c, all feature-preserving ETPF analysis particles exhibit a distinct wavefront. Particle 3 for the feature-preserving ETPF in Figure 16c shows fine-scale distortion, which is mainly because of the inherent weakness in the 2D alignment procedure (which, if we recall, naively aligns features independently in each direction). After thirty more assimilation cycles, the analysis particles for each method are shown in Figure 17. Figure 17b shows the standard ETPF particles, all of which have lost the wavefront feature. While subject to fine-scale distortion, the feature-preserving ETPF particles in Figure 17c still preserve their wavefront structure. Finally, Figure 18 shows the analysis densities at $t = 0.01$, where the standard ETPF has failed to preserve features, but the feature-preserving ETPF has preserved them, albeit with some minimal distortion.

5. Conclusions

This work develops a particle filtering methodology for performing physically faithful data assimilation with systems that develop features. The new “Feature-preserving ETPF” algorithm extends the standard ETPF by performing aligned optimal transportation. The methodology involves feature extraction (by taking the derivative of the density field), feature alignment (via dynamic time warping), and aligned transportation (via a special interpolation formula that accounts for feature alignment). The feature-preserving ETPF has been rigorously tested on four different test cases, three problems in 1D and one problem in 2D. All experiments are carried out with highly sparse observations of pressure. As long as the extracted feature profiles from all particles match, feature-preserving ETPF will not only estimate the correct states (and other derived

quantities of interest, such as the entropy) but also preserve features such as discontinuities.

As seen in the experiments, the feature-preserving ETPF provides qualitatively superior solutions because of its physically faithful approach to analysis. In the 2D experiment, the feature-preserving ETPF shows small-scale distortions (Figures 16 to 18) since the 2D alignment is computed independently in each dimension.

An important assumption for the feature-preserving ETPF is that the same solution features are present across all particles. When this assumption is not fulfilled, the feature-preserving ETPF may not preserve the features over multiple assimilation steps.

There are multiple directions for future work.

- (i) The features of multiple particles may not match in the following cases. Firstly, when a flow has reflective boundaries, and only a subset of particles have interacted with the said boundary, the profiles tend to be different. Secondly, when the uncertainties are large and the initial particles are sufficiently different, their evolved profiles could develop different sets of features. Thus, it is necessary to investigate feature-preserving ETPF methods when different particles exhibit different features at the same time instance.
- (ii) One possible solution to prevent artifacts in 2D could be to use a 2D-DTW method, which does not decouple the dimensions, such as [45, 57]. Otherwise, novel multi-dimensional sequence alignment techniques must be developed to solve this problem. This would also help scale the feature-preserving filtering methodology to realistic 3D problems.
- (iii) Discrete first order approximations of $\partial\rho/\partial x$ (for 1D) and $\partial^2\rho/\partial x\partial y$ (for 2D) has been successful for feature extraction and alignment. Other choices for better feature extraction could be explored.
- (iv) While not presented in the manuscript, experiments giving rise to tur-

bulence were also run in 2D. The turbulence gets averaged out in the analysis procedure, making the feature-preserving ETPF more applicable to unsteady averaged flows. More research needs to be done to perform feature alignment in turbulent settings.

Acknowledgement

We thank Prof. Jeff Borggaard from the Mathematics department at Virginia Tech for helpful discussions.

Funding: This work was supported by the Department of Energy, the National Science Foundation via awards DMS-2411069 and DMS-2436357, and by the Computational Science Laboratory at Virginia Tech.

References

- [1] M. Asch, M. Bocquet, M. Nodet, Data Assimilation, Society for Industrial and Applied Mathematics, Philadelphia, PA, 2016. `arXiv:https://epubs.siam.org/doi/pdf/10.1137/1.9781611974546`, `doi:10.1137/1.9781611974546`.
URL `https://epubs.siam.org/doi/abs/10.1137/1.9781611974546`
- [2] S. Reich, C. Cotter, Probabilistic forecasting and Bayesian data assimilation, Cambridge University Press, 2015.
- [3] G. Evensen, F. C. Vossepoel, P. J. van Leeuwen, Data assimilation fundamentals: A unified formulation of the state and parameter estimation problem, Springer Nature, 2022.
- [4] P. J. Van Leeuwen, Y. Cheng, S. Reich, P. J. van Leeuwen, Nonlinear Data Assimilation for high-dimensional systems: -with geophysical applications, Springer, 2015.
- [5] E. F. Toro, Flux Vector Splitting Methods, Springer Berlin Heidelberg, Berlin, Heidelberg, 2009. `doi:10.1007/b79761_8`.
URL `https://doi.org/10.1007/b79761_8`

- [6] G. Evensen, Sequential data assimilation with a nonlinear quasi-geostrophic model using Monte Carlo methods to forecast error statistics, *Journal of Geophysical Research* 99 (C5) (1994) 10143–10162.
- [7] B. G., van Leeuwen. P. J., E. G., Analysis scheme in the Ensemble Kalman Filter, *Monthly Weather Review* 126 (1998) 1719–1724.
- [8] P. Houtekamer, H. Mitchell, Data assimilation using an ensemble Kalman filter technique , *Monthly Weather Review* 126 (1998) 796–811.
- [9] P. Sakov, P. R. Oke, A deterministic formulation of the ensemble kalman filter: an alternative to ensemble square root filters, *Tellus A* 60 (2) (2008) 361–371. arXiv:<https://onlinelibrary.wiley.com/doi/pdf/10.1111/j.1600-0870.2007.00299.x>, doi:<https://doi.org/10.1111/j.1600-0870.2007.00299.x>.
URL <https://onlinelibrary.wiley.com/doi/abs/10.1111/j.1600-0870.2007.00299.x>
- [10] P. J. van Leeuwen, Particle filtering in geophysical systems, *Monthly Weather Review* 137 (12) (2009) 4089 – 4114. doi: 10.1175/2009MWR2835.1.
URL <https://journals.ametsoc.org/view/journals/mwre/137/12/2009mwr2835.1.xml>
- [11] P. J. van Leeuwen, H. R. Künsch, L. Nerger, R. Potthast, S. Reich, Particle filters for high-dimensional geoscience applications: A review, *Quarterly Journal of the Royal Meteorological Society* 145 (723) (2019) 2335–2365. arXiv:<https://rmets.onlinelibrary.wiley.com/doi/pdf/10.1002/qj.3551>, doi:<https://doi.org/10.1002/qj.3551>.
URL <https://rmets.onlinelibrary.wiley.com/doi/abs/10.1002/qj.3551>
- [12] P. J. Van Leeuwen, Nonlinear data assimilation in geosciences: an extremely efficient particle filter, *Quarterly Journal of the Royal Meteorological Society* 136 (653) (2010) 1991–1999.

- [13] F. Daum, J. Huang, A. Noushin, Exact particle flow for nonlinear filters, in: I. Kadar (Ed.), *Signal Processing, Sensor Fusion, and Target Recognition XIX*, Vol. 7697, International Society for Optics and Photonics, SPIE, 2010, p. 769704. doi:10.1117/12.839590.
URL <https://doi.org/10.1117/12.839590>
- [14] A. N. Subrahmanya, A. A. Popov, A. Sandu, Ensemble variational fokker-planck methods for data assimilation, *Journal of Computational Physics* (2024) 113681doi:<https://doi.org/10.1016/j.jcp.2024.113681>.
URL <https://www.sciencedirect.com/science/article/pii/S002199912400929X>
- [15] C.-C. Hu, P. J. van Leeuwen, J. L. Anderson, An implementation of the particle flow filter in an atmospheric model, *Monthly Weather Review* 152 (10) (2024) 2247 – 2264. doi:10.1175/MWR-D-24-0006.1.
URL <https://journals.ametsoc.org/view/journals/mwre/152/10/MWR-D-24-0006.1.xml>
- [16] A. N. Subrahmanya, A. A. Popov, R. J. Gomillion, A. Sandu, Preserving nonlinear constraints in variational flow filtering data assimilation (2024). arXiv:2405.04380.
URL <https://arxiv.org/abs/2405.04380>
- [17] S. Reich, A nonparametric ensemble transform method for bayesian inference, *SIAM Journal on Scientific Computing* 35 (4) (2013) A2013–A2024. arXiv:<https://doi.org/10.1137/130907367>, doi:10.1137/130907367.
URL <https://doi.org/10.1137/130907367>
- [18] M. A. Freitag, N. K. Nichols, C. J. Budd, Resolution of sharp fronts in the presence of model error in variational data assimilation, *Quarterly Journal of the Royal Meteorological Society* 139 (672) (2013) 742–757. arXiv:<https://rmets.onlinelibrary.wiley.com/doi/pdf/10.1002/qj.2002>, doi:<https://doi.org/10.1002/qj.2002>.

URL <https://rmets.onlinelibrary.wiley.com/doi/abs/10.1002/qj.2002>

- [19] A. Srivastava, W. Kang, D. M. Tartakovsky, Feature-informed data assimilation, *Journal of Computational Physics* 494 (2023) 112499. doi:<https://doi.org/10.1016/j.jcp.2023.112499>.

URL <https://www.sciencedirect.com/science/article/pii/S0021999123005946>

- [20] T. Li, A. Gelb, Y. Lee, A structurally informed data assimilation approach for nonlinear partial differential equations, *Journal of Computational Physics* 519 (2024) 113396. doi:<https://doi.org/10.1016/j.jcp.2024.113396>.

URL <https://www.sciencedirect.com/science/article/pii/S0021999124006442>

- [21] T. Houba, A. Edoh, R. Munipalli, M. E. Harvazinski, Sequential Data Assimilation in Flows with Shocks, *American Institute of Aeronautics and Astronautics*, 2024, Ch. 0587. arXiv:<https://arc.aiaa.org/doi/pdf/10.2514/6.2024-0587>, doi:10.2514/6.2024-0587.

URL <https://arc.aiaa.org/doi/abs/10.2514/6.2024-0587>

- [22] J. J. Hansen, D. Brouzet, M. Ihme, A Normal-Score Ensemble Kalman Filter for 1D Shock Waves, *American Institute of Aeronautics and Astronautics*, 2024, Ch. 1022. arXiv:<https://arc.aiaa.org/doi/pdf/10.2514/6.2024-1022>, doi:10.2514/6.2024-1022.

URL <https://arc.aiaa.org/doi/abs/10.2514/6.2024-1022>

- [23] A. Edoh, T. Houba, R. Munipalli, M. E. Harvazinski, Sequential Ensemble Kalman Filtering of Compressible Flows With Shocks: Enforcing Positivity, *American Institute of Aeronautics and Astronautics*, 2025, Ch. 0918. arXiv:<https://arc.aiaa.org/doi/pdf/10.2514/6.2025-0918>, doi:10.2514/6.2025-0918.

URL <https://arc.aiaa.org/doi/abs/10.2514/6.2025-0918>

- [24] E. J. West, J. F. MacArt, R. Munipalli, Variational Data Assimilation in Shock Tube Flows, American Institute of Aeronautics and Astronautics, 2025, Ch. 1166. arXiv:<https://arc.aiaa.org/doi/pdf/10.2514/6.2025-1166>, doi:10.2514/6.2025-1166.
URL <https://arc.aiaa.org/doi/abs/10.2514/6.2025-1166>
- [25] H. Sakoe, S. Chiba, Dynamic programming algorithm optimization for spoken word recognition, IEEE Transactions on Acoustics, Speech, and Signal Processing 26 (1) (1978) 43–49. doi:10.1109/TASSP.1978.1163055.
- [26] S. Ravela, K. Emanuel, D. McLaughlin, Data assimilation by field alignment, Physica D: Nonlinear Phenomena 230 (1) (2007) 127–145, data Assimilation. doi:<https://doi.org/10.1016/j.physd.2006.09.035>.
URL <https://www.sciencedirect.com/science/article/pii/S0167278906003551>
- [27] J. D. Beezley, J. Mandel, Morphing ensemble kalman filters, Tellus A: Dynamic Meteorology and Oceanography (Jan 2008). doi:10.1111/j.1600-0870.2007.00275.x.
- [28] S. Ravela, Quantifying uncertainty for coherent structures, Procedia Computer Science 9 (2012) 1187–1196, proceedings of the International Conference on Computational Science, ICCS 2012. doi:<https://doi.org/10.1016/j.procs.2012.04.128>.
URL <https://www.sciencedirect.com/science/article/pii/S1877050912002499>
- [29] D. R. Stratman, C. K. Potvin, L. J. Wicker, Correcting storm displacement errors in ensembles using the feature alignment technique (fat), Monthly Weather Review 146 (7) (2018) 2125 – 2145. doi:10.1175/MWR-D-17-0357.1.
URL <https://journals.ametsoc.org/view/journals/mwre/146/7/mwr-d-17-0357.1.xml>

- [30] L. Li, A. Vidard, F.-X. Le Dimet, J. Ma, Topological data assimilation using wasserstein distance, *Inverse Problems* 35 (1) (2018) 015006.
- [31] F.-X. Le Dimet, I. Souopgui, O. Titaud, V. Shutyaev, M. Y. Hussaini, Toward the assimilation of images, *Nonlinear Processes in Geophysics* 22 (1) (2015) 15–32. doi:10.5194/npg-22-15-2015.
URL <https://npg.copernicus.org/articles/22/15/2015/>
- [32] Y. Ying, A multiscale alignment method for ensemble filtering with displacement errors, *Monthly Weather Review* 147 (12) (2019) 4553 – 4565. doi:10.1175/MWR-D-19-0170.1.
URL <https://journals.ametsoc.org/view/journals/mwre/147/12/mwr-d-19-0170.1.xml>
- [33] Y. Ying, J. L. Anderson, L. Bertino, Improving vortex position accuracy with a new multiscale alignment ensemble filter, *Monthly Weather Review* 151 (6) (2023) 1387 – 1405. doi:10.1175/MWR-D-22-0140.1.
URL <https://journals.ametsoc.org/view/journals/mwre/151/6/MWR-D-22-0140.1.xml>
- [34] F. G. Operti, Interpolation strategy based on dynamic time warping, Master’s thesis, Universidade Federal do Ceará (2015).
- [35] G. Peyré, M. Cuturi, et al., Computational optimal transport: With applications to data science, *Foundations and Trends® in Machine Learning* 11 (5-6) (2019) 355–607.
- [36] G. A. Sod, A survey of several finite difference methods for systems of nonlinear hyperbolic conservation laws, *Journal of Computational Physics* 27 (1) (1978) 1–31. doi:[https://doi.org/10.1016/0021-9991\(78\)90023-2](https://doi.org/10.1016/0021-9991(78)90023-2).
URL <https://www.sciencedirect.com/science/article/pii/0021999178900232>

- [37] R. Tavenard, An introduction to dynamic time warping, <https://rtavenar.github.io/blog/dtw.html> (2021).
- [38] P. Senin, Dynamic time warping algorithm review, Information and Computer Science Department University of Hawaii at Manoa Honolulu, USA 855 (1-23) (2008) 40.
- [39] T. K. Vintsyuk, Speech discrimination by dynamic programming, Cybernetics 4 (1) (1968) 52–57. doi:10.1007/BF01074755.
URL <https://doi.org/10.1007/BF01074755>
- [40] M. Shokoohi-Yekta, B. Hu, H. Jin, J. Wang, E. Keogh, Generalizing DTW to the multi-dimensional case requires an adaptive approach, Data Min. Knowl. Discov. 31 (1) (2017) 1–31.
- [41] C. Banderier, S. Schwer, Why delannoy numbers?, Journal of Statistical Planning and Inference 135 (1) (2005) 40–54, special issue on lattice path combinatorics and discrete distributions. doi:<https://doi.org/10.1016/j.jspi.2005.02.004>.
URL <https://www.sciencedirect.com/science/article/pii/S0378375805000534>
- [42] F. Itakura, Minimum prediction residual principle applied to speech recognition, IEEE Transactions on Acoustics, Speech, and Signal Processing 23 (1) (1975) 67–72. doi:10.1109/TASSP.1975.1162641.
- [43] E. J. Keogh, M. J. Pazzani, Derivative Dynamic Time Warping, Society for Industrial and Applied Mathematics, 2001, Ch. 1, pp. 1–11. arXiv: <https://epubs.siam.org/doi/pdf/10.1137/1.9781611972719.1>, doi: 10.1137/1.9781611972719.1.
URL <https://epubs.siam.org/doi/abs/10.1137/1.9781611972719.1>
- [44] Z. Zhang, R. Tavenard, A. Bailly, X. Tang, P. Tang, T. Corpetti, Dynamic time warping under limited warping path length, Information Sciences 393 (2017) 91–107. doi:<https://doi.org/10.1016/j.ins.2017.02.018>.

URL <https://www.sciencedirect.com/science/article/pii/S0020025517304176>

- [45] H. Lei, V. Govindaraju, Direct image matching by dynamic warping, in: 2004 Conference on Computer Vision and Pattern Recognition Workshop, IEEE, 2004, pp. 76–76.
- [46] D. Hale, Dynamic warping of seismic images, *Geophysics* 78 (2) (2013) S105–S115.
- [47] M. Shokoohi-Yekta, J. Wang, E. Keogh, On the Non-Trivial Generalization of Dynamic Time Warping to the Multi-Dimensional Case, *Society for Industrial and Applied Mathematics*, 2015, Ch. 33, pp. 289–297. arXiv:<https://epubs.siam.org/doi/pdf/10.1137/1.9781611974010.33>, doi:10.1137/1.9781611974010.33.
URL <https://epubs.siam.org/doi/abs/10.1137/1.9781611974010.33>
- [48] G. S. Settles, *Basic Concepts*, Springer Berlin Heidelberg, Berlin, Heidelberg, 2001. doi:10.1007/978-3-642-56640-0.
URL <https://doi.org/10.1007/978-3-642-56640-0>
- [49] D. Ziou, S. Tabbone, Edge detection techniques-an overview, *Pattern Recognition and Image Analysis: Advances in Mathematical Theory and Applications* 8 (4) (1998) 537–559.
- [50] P. Thévenaz, T. Blu, M. Unser, 25 - image interpolation and resampling, in: I. N. BANKMAN (Ed.), *Handbook of Medical Imaging, Biomedical Engineering*, Academic Press, San Diego, 2000, pp. 393–420. doi:<https://doi.org/10.1016/B978-012077790-7/50030-8>.
URL <https://www.sciencedirect.com/science/article/pii/B9780120777907500308>
- [51] C.-W. Shu, S. Osher, Efficient implementation of essentially non-oscillatory shock-capturing schemes, ii, *Journal of Computational Physics* 83 (1) (1989) 32–78. doi:[https://doi.org/10.1016/0021-9991\(89\)90222-2](https://doi.org/10.1016/0021-9991(89)90222-2).

URL <https://www.sciencedirect.com/science/article/pii/S0021999189902222>

- [52] G.-S. Jiang, C.-W. Shu, Efficient implementation of weighted eno schemes, *Journal of Computational Physics* 126 (1) (1996) 202–228. doi:<https://doi.org/10.1006/jcph.1996.0130>.

URL <https://www.sciencedirect.com/science/article/pii/S0021999196901308>

- [53] S. Gottlieb, C.-W. Shu, Total variation diminishing Runge-Kutta schemes, *Mathematics of computation* 67 (221) (1998) 73–85.

- [54] M. A. Diaz, `wme7/approximateRiemannSolvers`, GitHub (2025).

URL <https://github.com/wme7/ApproximateRiemannSolvers>

- [55] R. Zanetti, K. J. DeMars, R. H. Bishop, Underweighting nonlinear measurements, *Journal of Guidance, Control, and Dynamics* 33 (5) (2010) 1670–1675. arXiv:<https://doi.org/10.2514/1.50596>, doi:10.2514/1.50596.

URL <https://doi.org/10.2514/1.50596>

- [56] P. R. Woodward, Trade-offs in designing explicit hydrodynamical schemes for vector computers**work performed in part under the auspices of the u.s. department of energy by the lawrence livermore national laboratory under contract number w-7405-eng-48 and by the office of basic energy sciences., in: G. RODRIGUE (Ed.), *Parallel Computations*, Academic Press, 1982, pp. 153–171. doi:<https://doi.org/10.1016/B978-0-12-592101-5.50011-7>.

URL <https://www.sciencedirect.com/science/article/pii/B9780125921015500117>

- [57] C. Gao, J. Li, W. Shen, P. Yin, Two-dimensional dynamic time warping algorithm for matrices similarity, *Intelligent Data Analysis* 26 (4) (2022) 859–871. arXiv:<https://journals.sagepub.com/doi/pdf/10.>

3233/IDA-215908, doi:10.3233/IDA-215908.

URL <https://journals.sagepub.com/doi/abs/10.3233/IDA-215908>